BRNO UNIVERSITY OF TECHNOLOGY
VYSOKÉ UČENÍ TECHNICKÉ V BRNĚ

FACULTY OF MECHANICAL ENGINEERING
FAKULTA STROJNÍHO INŽENÝRSTVÍ

INSTITUTE OF PHYSICAL ENGINEERING
ÚSTAV FYZIKÁLNÍHO INŽENÝRSTVÍ

MODULE FOR THE DETECTION OF LIGHT ELEMENTS IN FERROUS ALLOYS BY THE LASER-INDUCED BREAKDOWN SPECTROSCOPY TECHNIQUE

MODUL PRO DETEKCI LEHKÝCH PRVKŮ V ŽELEZNÝCH SLITINÁCH METODOU SPEKTROSKOPIE LASEREM BUZENÉHO PLAZMATU

MASTER'S THESIS
DIPLOMOVÁ PRÁCE

AUTHOR — **Bc. Zdeněk Hrabal**
AUTOR PRÁCE

SUPERVISOR — **Ing. Jan Novotný, Ph.D.**
VEDOUCÍ PRÁCE

BRNO 2018

BRNO UNIVERSITY OF TECHNOLOGY
FACULTY OF MECHANICAL ENGINEERING

Master's Thesis Assignment

Institut:	Institute of Physical Engineering
Student:	**Bc. Zdeněk Hrabal**
Degree programm:	Applied Sciences in Engineering
Branch:	Precise Mechanics and Optics
Supervisor:	**Ing. Jan Novotný, Ph.D.**
Academic year:	2017/18

As provided for by the Act No. 111/98 Coll. on higher education institutions and the BUT Study and Examination Regulations, the director of the Institute hereby assigns the following topic of Master's Thesis:

Module for the detection of light elements in ferrous alloys by the Laser-Induced Breakdown Spectroscopy technique

Brief description:

Laser-Induced Breakdown Spectroscopy usually deals with the spectral range of 250-800 nm, where the emission lines of the most of the chemical elements can be found. Detection of the crucial light elements in ferrous alloys requires in many cases the detection capability in VUV region below the 200 nm. The transmission of the Air and most commonly used optical materials, including Si-based optical fibers, is insufficient in this spectral region. A special design of the detection module is therefore necessary.

Master's Thesis goals:

The primary goal of this thesis is to design, develop and test a module for the LIBS analysis of iron alloys in the spectral range under the 200 nm called Vacuum Ultraviolet (VUV). The module will consist of optomechanical components, a spectrometer, and collection optics, which will focus the plasma's radiation onto the slit of the spectrometer.

The crucial issue will be an absorption of the VUV radiation by air which excludes the possibility of using conventional optics or optical fibers. Therefore, the whole system will also have to be purged with argon.

The work also includes a research of state of the art in terms of VUV analysis by LIBS, commercially available VUV spectrometers and designs of such devices.

Recommended bibliography:

KHATER, M. A. Laser-induced breakdown spectroscopy for light elements detection in steel: State of the art. Spectrochimica Acta Part B: Atomic Spectroscopy, Volume 81, 2013, Pages 1-10, ISSN 0584-8547, https://doi.org/10.1016/j.sab.2012.12.010.

MIZIOLEK, A. W., PALLESCHI, V., SCHECHTER, I. (ed.). Laser induced breakdown spectroscopy. Cambridge University Press, 2006.

Students are required to submit the thesis within the deadlines stated in the schedule of the academic year 2017/18.

In Brno, 26. 10. 2017

VYSOKÉ UČENÍ TECHNICKÉ V BRNĚ
FAKULTA STROJNÍHO INŽENÝRSTVÍ
DĚKANÁT
L. S.

prof. RNDr. Tomáš Šikola, CSc.
Director of the Institute

doc. Ing. Jaroslav Katolický, Ph.D.
FME dean

ABSTRACT

This diploma thesis' aim is an investigation of light elements (i.e. carbon, sulphur and phosphorus) in ferrous alloys using Laser-Induced Breakdown Spectroscopy (LIBS). The primary goal is both the development and implementation of the new module enabling an analysis of vacuum ultraviolet (VUV) radiation which is necessary for the steel analysis and also more applications of LIBS.

The first part surveys the state-of-the-art approaches of optical emission spectroscopy (OES), as well as the overview of traditional techniques used for steel analyse. The theory concerning the absorption of VUV by the air and optical glasses has been also investigated in order to get the essential theoretical background for the development of the module.

The experimental module was carried out prior to the final design in order to test the concept of the VUV analysis by LIBS. On the basis of this testing, the final design was proposed based on the unique wedge mechanism. The prototype was made up in cooperation with an external manufacturer and then the performances of the module were demonstrated by measurements of five certified steel standards. The experiments determined the limit of detection for carbon as $0.028\ \mathrm{wt.\%}$. Nevertheless, neither sulphur nor phosphorus were detected in any of studied sample.

This thesis establishes the essential know-how for further investigation of the VUV-LIBS analysis in the Laboratory of laser spectroscopy in Brno.

KEYWORDS

Laser-Induced Breakdown Spectroscopy (LIBS), precise mechanics, collection optics, Vacuum ultraviolet, laser, plasma

ABSTRAKT

Tato diplomová práce je zaměřena na analýzu lehkých prvků (tj. uhlík, sýra a fosfor) v železných slitinách pomocí metody laserem indukovaného plazmatu (LIBS). Hlavním cílem je vyvinout a implementovat nový modul, který bude umožňovat analýzu v hluboké ultrafialové oblasti (VUV), což je nezbytné jak pro stanovení chemického složení lehkých prvků v ocelích tak pro mnoho dalších aplikací metody LIBS.

V první části je vytvořen přehled moderních přístupů optické emisní spektroskopie (OES) a rovněž jsou shrnuty tradiční techniky používané v metalurgii pro analýzu ocelí. Teorie absorpce ultrafialového záření vzduchem a optickými skly byla důkladně studována a shrnuta k získání potřebného teoretického základu k vývoji modulu.

Před návrhem finální verze modulu byl navržen experimentální modul s cílem otestovat navržený koncept analýzy ve VUV oblasti metodou LIBS. Na základě testování byla navrhnuta finální verze založená na unikátním klínovém mechanismu. Funkční vzorek byl vyroben ve spolupráci s extérním výrobcem a vlastnosti modulu byly následně demonstrovány naměřením pěti certifikovaných ocelových standardů. Experiment určil limity detekce pro uhlík jako $0.028\ \mathrm{hm.\%}$. Nicméně, síra ani fosfor nebyly detekovány v žádném ze vzorků.

Tato práce vytvořila modul nezbytný pro budoucí zkoumání metody LIBS v oblasti VUV v Laboratoři laserové spektroskopie v Brně.

KLÍČOVÁ SLOVA

Spektroskopie laserem indukovaného plasmatu, jemná mechanika, sběrná optika, Vakuum ultrafialové záření, laser, plazma

HRABAL, Zdeněk. *Module for the detection of light elements in ferrous alloys by the Laser-Induced Breakdown Spectroscopy technique*. Brno, Rok, 83 p. Master's Thesis. Brno University of Technology, Faculty of Mechanical Engineering, Department of Physical Engineering. Advised by Ing. Jan Novotný, Ph.D

DECLARATION

I declare that I have written the Master's Thesis titled "Module for the detection of light elements in ferrous alloys by the Laser-Induced Breakdown Spectroscopy technique" independently, under the guidance of the advisor and using exclusively the technical references and other sources of information cited in the thesis and listed in the comprehensive bibliography at the end of the thesis.

As the author I furthermore declare that, with respect to the creation of this Master's Thesis, I have not infringed any copyright or violated anyone's personal and/or ownership rights. In this context, I am fully aware of the consequences of breaking Regulation § 11 of the Copyright Act No. 121/2000 Coll. of the Czech Republic, as amended, and of any breach of rights related to intellectual property or introduced within amendments to relevant Acts such as the Intellectual Property Act or the Criminal Code, Act No. 40/2009 Coll., Section 2, Head VI, Part 4.

Brno ....

author's signature

ACKNOWLEDGEMENT

I would like to express my thank to Ing. Jan Novotný, Ph.D for his help and guidance throughout all phases of this work. I would like to also appreciate the positive and co-operative attitude of all members of Laboratory of laser spectroscopy in Brno. Particularly, my special thanks to Ing. Michal Brada for his factual comments concerning the mechanical design, Ing. Lukáš Novák for his help with the electronics, and, last but not least, Ing. Pavel Pořízka, Ph.D., the head of Laboratory of laser spectroscopy in Brno, for his advice about the experimental aspects of this thesis.

Brno ....

author's signature

Contents

List of Figures

List of Tables

Introduction

An analysis of the light elements in the iron alloys has been challenging in secondary metallurgy for a very long time and still researchers are trying to find a modern technique which would be able to overcome the main drawbacks of the current methods.

Metallurgists are greatly interested in the light elements including carbon, phosphorus, sulfur and hydrogen. Carbon is the most crucial element in the ferrous alloys because it forms a crystallographic structure of iron and thus significantly influences the mechanical properties of steel [1]. Phosphorus, sulfur, and hydrogen are impurities that negatively affect the properties of steel. As far as we know, the only exception is a use of sulfur in the foundry industry which positively influences the wettability of cast iron during casting. These impurities should be carefully monitored in the order of μg/g because even a trace concentration of P and S can play a major role in the embrittlement of steel during tempering . A trace concentration of As and Sb has the same effect [2]. This phenomenon is called temper embrittlement or tempered martensite embrittlement.

An analysis of light elements in the iron alloys is very challenging. For instance, the well-known spectroscopic method X-ray fluorescence (XRF) has a great difficulty detecting any element with a proton number under 22 (titanium). Therefore XRF is not appropriate for the C, P, S, etc. analysis. Spark Discharge Optical Emission Spectrometry (SP-OES) and absorption spectroscopy of analytes in flames are the only convenient methods in secondary metallurgy so far. They achieve the limits of detection under one μg/g for almost every element but they also have drawbacks including demanding sample preparation and time-consuming analysis.

Laser Induced Breakdown Spectroscopy (LIBS) is an atomic emission spectroscopy based on the detection of plasma radiation excited by laser ablation [3, 4, 5]. This method's performance is comparable to other techniques as for the analysis of light elements in steel. The limit of detection (LOD) of C, P, and S under the range of ten μg/g was achieved for the first time by V. Sturm at 2000 [6]. M. Hemmerlin compared LIBS with SD-OES in his work from 2001 [7] and he obtained comparable LOD for C, P, and S. Furthermore, LIBS technique's unique capabilities are following: a remote analysis, no sample preparation, analysis of the solid as well as liquid state, simple setup, etc. Noll [8] estimated that LIBS is two times faster than some conventional techniques which can significantly reduce the price of the steelmaking process. Therefore, LIBS is the promising alternative in the steelmaking process regarding a lower cost and a faster analysis.

However, the majority of ordinary LIBS devices that are able to analyze UV-VIS-NIR spectral range are not capable of monitoring the light elements in steel

because none emission can be detected in this range of wavelength. The reasons for that are going to be discussed in chapter 5.1. Thus, most of researchers investigated steels in the Vacuum Ultraviolet (VUV) spectral range (i.e. below 200 nm) which requires a special instrumentation due to the absorption of VUV radiation by air as well as optical glasses [6, 7, 9, 10].

Devices available in the Laboratory of laser spectroscopy in Brno are capable of doing a comprehensive LIBS analysis including the high resolution and fast chemical mapping, multi-pulse techniques and so on. Nevertheless, the main experimental setup is limited to the spectral range of UV-VIS-NIR and hence the light elements in steel cannot be investigated. The primary goal of this thesis is to develop, test and implement a module that enhances the detectable range up to wavelengths below 200 nm. The module shall be compatible with a standard mounting and with the modular system of devices in the laboratory, particularly with the interaction chamber. A comprehensive research concerning the steel analysis in VUV shall be outlined prior to the development of the new module. The performances of the module will be demonstrated on measurements of several steel samples and LOD for carbon will be determined.

Even though the analysis in VUV regards mainly the determination of light elements in steel, some applications of LIBS in VUV has also been found in pharmaceutical industry [11], in the detection of trace elements in polymers [12] or even in the human exploration of Mars [13]. Therefore the development and implementation of the VUV module will open up some new possibilities of analysis for the research group of laser spectroscopy in Brno.

1 State of the art

1.1 Traditional techniques of the steel analysis

Iron and ferrous alloys used to be analysed mainly by colorimetry and by other "wet chemical" techniques, which requires difficult chemical procedures including dissolution of the steel sample and consequently separation of the analyte by precipitation. These techniques achieve high sensitivity and accuracy but obviously, they are time-consuming and they require well-equipped chemical laboratory for such complex chemical procedures. [14]

Therefore, most of the techniques currently used in the metallurgy are based on a spectroscopic device that is calibrated by steel standards with well-defined chemical composition. Optical emission spectroscopy (OES) as well as optical absorption spectroscopy (OAS) plays important role in steel industry. OAS is usually associated with the combustion of dissolution of the analyte. In metallurgy, the atoms included in the sample are investigated rather than chemical bonds so that the techniques are also referred as Atomic Absorption/Emission Spectroscopy (AAS/AES [1]). So, when we need the light to interact with the sample's atoms, the raw material of the sample must be atomized by heat in form of either arc, spark, flame or plasma. Each excitation source has its particular advantages as well as disadvantages, which we are going to briefly outline in the next sections.

The technique of combustion of the analyte in a flame is one of the most sensitive and precise methods enabling analysis of trace concentrations of light elements in steel. The combustion of the sample in a stream of oxygen yields CO_2 as well as SO_2 produced in the flame. These gases are typically measured by the infrared absorption spectroscopy in order to quantitatively reveal the C and S concentration in a steel sample. This technique is used for instance in the verification of finished product analyses. On the contrary, it is rather not the appropriate technique in the process control.

The leader among the rapid techniques for process control in steel industry remains the optical emission spectroscopy, especially the Spark-Discharge OES (SD-OES) has been very popular technique. Particularly, this is evident from the range of the commercial devices that are proposed for the steel process control by the leading manufacturers of the spectroscopic devices such as Thermo Fisher or Bruker. These devices achieve LOD less than 10 μg/g [15] for almost every element needed to be analysed in steel, which ought to be sufficient in steel process control. The sample preparation comprises only the milling and polishing of the sample's surface. This

[1] The term AES for Atomic Emission Spectroscopy is not widely used because the abbreviation AES is rather known for Auger Electron Spectroscopy.

is the advantage in comparison with other techniques of OES, although there is also a technique with much easier sample preparation procedure such as LIBS discussed in chapter 1.2.3. A disadvantage of the SD-OES is that the inhomogeneity of the solid-state sample can affect accuracy and reliability of the analysis. Therefore, the devices analysing homogeneous dissolution of the analyte such as Inductively Coupled Plasma Atomic Emission Spectroscopy (ICP-AES) achieve better results in terms of figure of merit. On the other hand, they are time-consuming and more expensive.

1.2 Optical Emission Spectroscopy

Optical Emission Spectroscopy (OES) is a broad group of techniques investigating the chemical composition of a sample by the interaction of the light with the matter. The techniques among the OES are based on a certain source exciting atoms, ions or molecules of a sample, which produces visible or invisible radiation. This radiation is then dispersed into a spectrum by the spectrometer and such a distribution of wavelengths is analysed in order to qualitatively or quantitatively reveal the chemical or structural composition of the sample. This chapter aims to examine basic principles of the optical systems of OES. Particular attention will be paid to a technique using laser ablation known as Laser-induced Breakdown Spectroscopy (LIBS).

1.2.1 Spectrometers

A spectrometer is a device dispersing the light into its spectrum that provides an information about the intensity of wavelengths. The elder spectrometers used prisms as a dispersive element but they became obsolete once the diffraction grating was invented. One can imagine the diffraction grating as a slit interferometer with a large number of slits; usually with tens of thousands. In the centre of the grating's symmetry, where all wavelengths interfere constructively, appears a bright line called zero-order. In other orders, each wavelength interferes in slightly different angle, which can be measured. A diffraction grating can be designed either as a reflective or transmissive [16].

The main reason, why the diffraction gratings are more popular than prisms in spectrometry, is their huge flexibility in terms of its resolving power, deviation angle or range of wavelength λ that is reflected (or transmitted). These properties can be easily determined by a proper combination of number of illuminated grooves N, a diffraction order m and a substrate of the grating. The resolving power $\frac{\lambda}{\mathrm{d}\lambda}$ of a

diffraction grating is given by

$$\frac{\lambda}{\mathrm{d}\lambda} = mN. \tag{1.1}$$

In the other hand, properties of a prism are determined by its glass and geometry, which quite limits the flexibility of the design. Assuming a prism, from which the ray of light is leaving under the minimal deviation angle [2] , the resolving power can be expressed as:

$$\frac{\lambda}{\mathrm{d}\lambda} = b\left|\frac{\mathrm{d}n}{\mathrm{d}\lambda}\right|, \tag{1.2}$$

where b is the base length of a prism and $\left|\frac{\mathrm{d}n}{\mathrm{d}\lambda}\right|$ is the slope of dispersion relation of the glass.

It is plain to see from equations (1.1) and (1.2) that the resolving power of prisms depends on a wavelength (shorter wavelength gives higher resolving power) because the dispersion relation depends on wavelength as well. This is the further advantage of gratings because their resolving power is independent of wavelengths. Furthermore, the gratings attain much greater resolution and better throughput for ultraviolet than prisms. The only drawback of diffraction gratings against prisms was their susceptibility to ghosts in the spectrum that are caused by periodic errors in the ruled grating pattern [17]. Nevertheless, this drawback has been overcome by holographic gratings that are free of periodic errors.

It is important to notice that the resolving power determined by equations (1.1) and (1.2) does not indicate very much about a resolving power of the spectrometer as a comprehensive device because the resolving power is affected also by the focal distance of the spectrometer f, by optical aberrations of the optical system, by the width of entrance slit w_{in} and by width of the pixel in detector w_{out}. Evaluation of resolving power combining all these parameters is the difficult task and it is not possible to express the theory in a single fundamental equation. One of the theory says, that the resolution power is determined as a Full Width At Half Maximum (FWHM) of the instrumental profile, which can be calculated as the convolution of the individual contribution from the images of the entrance slit, exit slit and the dispersion profile of the grating. [18]

Moreover, the resolving power is certainly not the only important parameter of spectrometers. Another important parameter indicating the power of the spectrometer is f/number (also called focal ratio or speed) that determines the throughput

[2] Deviation angle is the angle between the incident ray and the refracted ray, which leaves the prism.

[3] of the spectrometers and is defined as

$$f_{\#} = \frac{f}{W}, \tag{1.3}$$

where W is the width of the grating. [16]

There are many types of spectrometers based on different principles. Basically, they can be divided into two main categories, Dispersive and Fourier-transform spectrometers. The dispersive spectrometers rely on a diffraction grating that disperses the light into various directions that are focused on a detector. The most popular spectrometers in OES of this kind include Czerny-Turner, Echelle, and Paschen-Runge. Fourier-transform spectrometers use different principles and they are based on certain type of an interferometer. They detect a superposition of two branches of light that interfere each other and convert this information into the frequency domain by Fourier transformation. There are two main representatives called simply Fourier-transform Spectrometer and Spacial Heterodyne Spectrometer (SHS).

Czerny-Turner Spectrometer

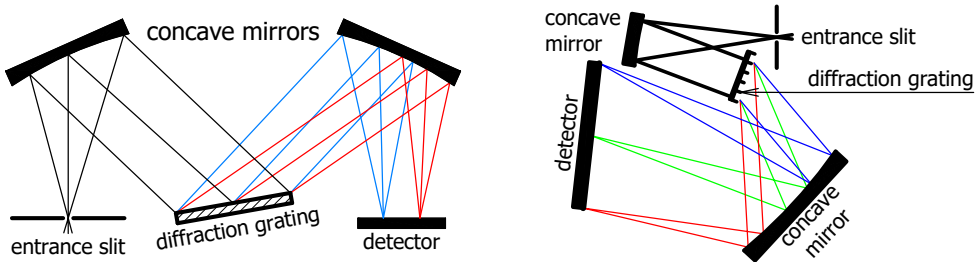

Fig. 1.1: Scheme of Czerny-Turner spectrometer. Traditional form of this spectrometer using reflective diffraction grating is in the left portion of this figure. Alternative form using transmissive grating is in the right portion of this figure.

Czerny-Turner is one of the simplest forms of a spectrometer. The left portion of Fig. 1.1 shows a traditional configuration of this spectrometer, which uses reflective diffraction grating as the dispersive element. A necessary part of the Czerny-Turner is collimating optics comprised two concave mirrors. The first one, placed in front of the grating, collimate the light passing through the entrance slit onto the grating and the second one focuses the dispersed light either onto a detector or, in case of a monochromator, onto an exit slit. The grating is usually mounted on a motorized turret that allows the shift of the spectral range by rotating with the grating. In

[3] In this case, the throughput stands for the relative intensity of the overall amount of light that is able to get through the spectrometer.

comparison with other dispersive spectrometers, Czerny-Turner has low f/number (high throughput) but the spectral range is usually narrow for high resolution.

The right portion of Fig. 1.1 depicts spectrometer using transmissive diffraction grating. This is not properly Czerny-Turner. However, it uses the same principles as the classical Czerny-Turner, although the configuration looks different. This spectrometer is profitable due to its compact dimensions.

Paschen-Runge Spectrometer

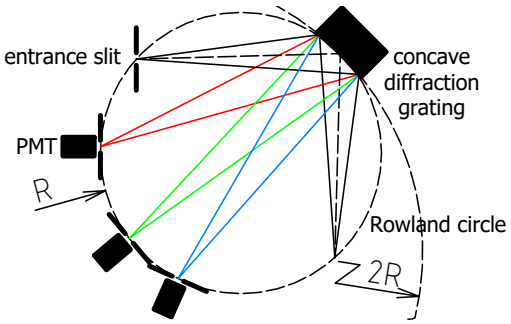

Fig. 1.2: Scheme of paschen-runge spectrometer.

Paschen-Runge is the most popular spectrometer with concave diffraction grating (see Fig. 1.2). The entrance slit, as well as exit slits, are placed on the circle called Rowland circle with radius R. The concave grating with a radius of $2R$ is tangential to the Rowland circle. This geometry ensures that the pencil of light from the entrance slit is focused by the concave shape of the grating onto the Rowland circle. Naturally, the zero order, containing full spectrum, is reflected in the angle of the geometrical reflection and focused on the certain position on the circle, which can be used as a virtual entrance slit by placing a flat mirror in this position. Other wavelengths of non-zero order are focused on different positions where they are selected by exit slits and detected usually by Photomultiplier tube (PMT) or photodiode. Therefore, the spectrum is not detected simultaneously but only by separated channels. Thus, Paschen-Runge is also called polychromator. This is the drawback of this spectrometer because the number of channels is limited. On the other hand, these separated channels are also advantageous because the channels have high sensitivity. Moreover, they are independent each other, meaning each channel can be set up individually in terms of sensitivity and gate delay.

A further significant advantage is an absence of any optical components except the concave grating. This feature makes Paschen-Runge the best spectrometer for a detection of Vacuum Ultraviolet because the grating can reflect wavelengths even under 100 nm.

On the contrary, a drawback of this spectrometer is its size. Usually, the focal length is around $f = 250$ mm in order to achieve sufficient resolution. The photomultipliers are also relatively expensive in comparison with ICCD or sCMOS.

Echelle Spectrometer

Equation (1.1) shows that the resolution of the grating can be gained if the number of groves or the diffraction order rises. To increase the number of groves is not the best solution because there is a limitation on the size of the grating. Diffraction order in common gratings should not be higher than two because higher orders have lower intensity due to diffraction on its tiny slits that modulates the resultant intensity of the spectrum. Moreover, high orders often do not exist because the grating equation does not have a solution for all orders. [4]

The grating providing hight diffraction orders, sometimes beyond $m = 100$, was suggested by Harrison in 1949 [19] in form of Echelles. This Low period reflective grating (usually from 30 to 300 grooves/mm) is tilted almost in Littrow condition [5] . Thus the diffraction order is increased due to the differences in the optical path between the pencils of light reflected by the particular grooves. On the other hand, all orders are significantly overlapped each other and thus have to be separated by further dispersive element, like grating or prism, placed either in front of or past the echelle grating. This element disperses the beam of light in a direction perpendicular to the diffracted light by the Echelle, which makes a 2D image called echellogram. Further information concerning Echelles and the related spectrometers can be found in [16, 20].

Echelle spectrometers have a broad spectral range covering the whole UV-VIS-NIR region with high resolution. Its dimensions are also quite small because the focal length does not have to be as long as in the case of other dispersive spectrometers. On the other hand, the throughput is lower and the calibration of the echellogram is not a trivial task.

Fourier-transform Spectrometer

Fourier-transform Spectrometers are based on completely different principles than the dispersive ones. Instead of dispersing the wavelengths to different positions, the wavelengths interfere and form a diffraction pattern representing the spectrum

[4] Grating equation is given by $m\lambda = d(\sin\alpha + \sin\beta)$, where α and β are incident and reflected angle with respect to grating normal, respectively. One can easily deduce that this equation does not have a real solution for all diffraction orders m.

[5] Littrow condition is satisfied when $\alpha = \beta$, where α and β are incident and reflected angle with respect to grating normal, respectively

in a spatial domain, which can be transformed into a frequency domain (spectrum of the plasma) by Fourier transform. Two main principles have been developed so far. Both of them rely on an interferometer, in most cases on the Michaelson interferometer. The traditional form, used mainly in infrared absorption spectroscopy, periodically moves with the flat mirror of the reference optical branch in Michaelson interferometer. Once the movable sensitive parts are necessary in this form of spectrometers, they are not very appropriate for an application of time-dependent spectroscopy.

The drawback of movable parts has been overcome by Spacial Heterodyne Spectrometer (SHS), which replaces the mirrors of the interferometer by the diffraction grating. The SHS excel in high throughput because it does not need a narrow slit to achieve high resolution. The further benefit is high durability because it can be designed as a small and monolithic device and thus the SHS is very convenient for astronomical and space applications [21]. Even ultraviolet can be detected by all-reflection construction of SHS [22]. The application of SHS has also been found in remote LIBS devices [23].

1.2.2 Laser in spectroscopy

Since the laser was invented by Gordon Gould and and Theodore Harold Maiman [24], many breakthroughs have been reported in physics. Naturally, scientists started to think about the applications of lasers in spectroscopy. For instance, a development of near-infrared lasers and CCD cameras introduced Raman spectroscopy into the "real-world" chemical analysis after 1986 [25]. This non-destructive technique uses detection of inelastic scattering of the laser and hence can reveal chemical bonds in the sample but the atomic structure of the sample cannot be quantified.

On the contrary, the laser beam of high power pulsed laser, when focused on the surface of the sample, can ablate, vaporize, atomize and ionise a small amount of its material. There are two techniques of spectroscopy that rely on this laser ablation including Laser Ablation Inductively Coupled Plasma Mass Spectrometry (LA-ICP-MS) and Laser-Induced Breakdown Spectroscopy (LIBS). Regarding LA-ICP-MS, the ions are transported by an inert gas stream to ICP-MS device and to the mass spectrometer in which they are separated and detected. LA-ICP-MS is accurate and extremely sensitive, with LOD in order of ppb but the mass spectrometers are expensive [26].

1.2.3 Laser-induced Breakdown Spectroscopy (LIBS)

LIBS does not measure the mass of the ions like LA-ICP-MS. Instead, this technique detects photons that are excited during plasma's lifetime and measures their energy

(wavelength). According to the quantum theory, this emitted energy in form of light is uniquely defined by the energy levels of atoms, ions or molecules because they can exist only in certain discrete states [27]. The exact energy emitted during certain excitation process that occurs between two states of energy E_1 and E_0 is given by the equation:

$$E_1 - E_0 = \frac{hc}{\lambda}, \tag{1.4}$$

where h is Planck constant, c is the speed of light and λ is the wavelength that is emitted. Therefore, the spectrum of the plasma's radiation comprises many strong peaks indicating a respective element in the sample and thus the spectrum is like a fingerprint of the chemical composition of the sample. Besides the emission peaks, the intense background caused by breaking radiation (bremsstrahlung) appears in a spectrum.

Although the processes occurring in the ablated material during the plasma's lifetime are very complicated, the basic principle of LIBS is quite simple. Every LIBS optical system relies on a nanosecond or a femtosecond pulsed laser with the pulse energy of typically from 1 to 1000 mj [5].The collimated radiation of the laser is then focused onto the surface of the sample by focusing lens so that the spot size on the surface can be very small and hence the irradiance can be extremely high. In the other words assuming the laser beam as a wave, the Gaussian laser beam with the size of the waist of w_{01} propagating through a thin lens is transformed into a Gaussian beam with a waist of the size of w_{02}. [28]

$$w_{02} = \frac{2\lambda f}{\pi w_{01}}, \tag{1.5}$$

where f is the focal length of the thin lens and λ is the wavelength of the laser beam. Assuming relatively big waist w_{01} in comparison with the focal length f, the waist w_{01} (i.e. the spot size) can be very small. This assumption can be easily satisfied for a beam leaving a laser. Of course, the lens is never perfect and the spot size is always affected by optical aberrations and the diffraction limitation. Nevertheless, the equation (1.5) gives a good approximation and tells us that the spot size is always the function of the focal length and the wavelength. The typical spot diameter is in order of 0.1 mm^2 [29]. This provides the irradiance in order of gigawatt per square centimetre, which ought to be enough for the excitation of the plasma.

The next step is to collect the radiation of the plasma and get the information about its spectrum. Most of LIBS devices use a collecting lens that images the plasma on the aperture of an optical fibre. The radiation is introduced by the fibre into the spectrometer, which disperses the light into the spectrum. There are many types of them that have been discussed in chapter 1.2.1. This collecting

system is easy and very convenient for UV-VIS-NIR radiation. It shall be discussed in detail in chapter 2. The plasma can be also imaged directly onto the slit of the spectrometer. For instance, the hand-held analysers or devices collecting VUV radiation (i.e. wavelengths under 200 nm) [30] are usually built on this principle. This technique has, however, difficulties related to adjustment (see chapter 2).

A very important feature of LIBS that must be noted is that the spectrum is significantly dependent on the time section in which the plasma is detected and integrated after the excitation. These parameters are usually labeled as gate delay (GD) and gate time (GT). The GD is a length of time between the excitation of the plasma and the opening of the detector's shutter. The GT is subsequent to the GD and determines the exposure time of a detector. The time-dependency of the LIBS means that the spectrum rapidly alternates during the plasma's lifetime. The early phase of a plasma (usually dozens of nanoseconds after the excitation) emits both the emission lines of the elements and besides, a bright continuum among the whole spectrum caused by the bremsstrahlung [3]. Weaker lines become visible later (usually hundreds of nanoseconds or more). Therefore, the radiation is usually not integrated among the whole excitation but rather it is time-resolved in order to improve the signal to noise ratio. However, this requires sophisticated electronics and extremely fast shutters of the detectors, since the plasma's lifetime is usually no longer than dozens of microseconds. Moreover, the signal is usually weak because only the small part of the radiation is collected.

The proper synchronisation of devices has been solved by delay generators, which periodically generate short electrical pulses delayed among each other very precisely. These pulses are used for synchronisation of the flash lump and Q-switch of the laser, the shutter of the detector and other devices. Regarding the extremely fast triggering of detector shutter and weak signal to detect, the intensified CCD and more recently CMOS cameras have been used.

LIBS also faces a problem related to interference of the emission lines caused by various of broadening mechanisms. The theory of spectrometers discussed in chapter 1.2.1 suggests that two or more wavelengths cannot be distinguished by a spectrometer when they are closer each other than the resolution of the spectrometer. In practice, it means that even perfect monochromatic source of light appears on the detector of the spectrometer as nonmonochromatic. In the other words, an infinitesimally narrow emission line is broadened by so-called instrumental broadening which has Gaussian distribution. Emission lines of plasma's radiation are not infinitesimally narrow either. Two main mechanisms participating in the broadening have been observed. First - Doppler broadening - is caused by chaotic movements of particles in the hot plasma so the Doppler effect occurs and thus it has also Gaussian distribution. Second - the Lorentz broadening - also called as pressure or collision

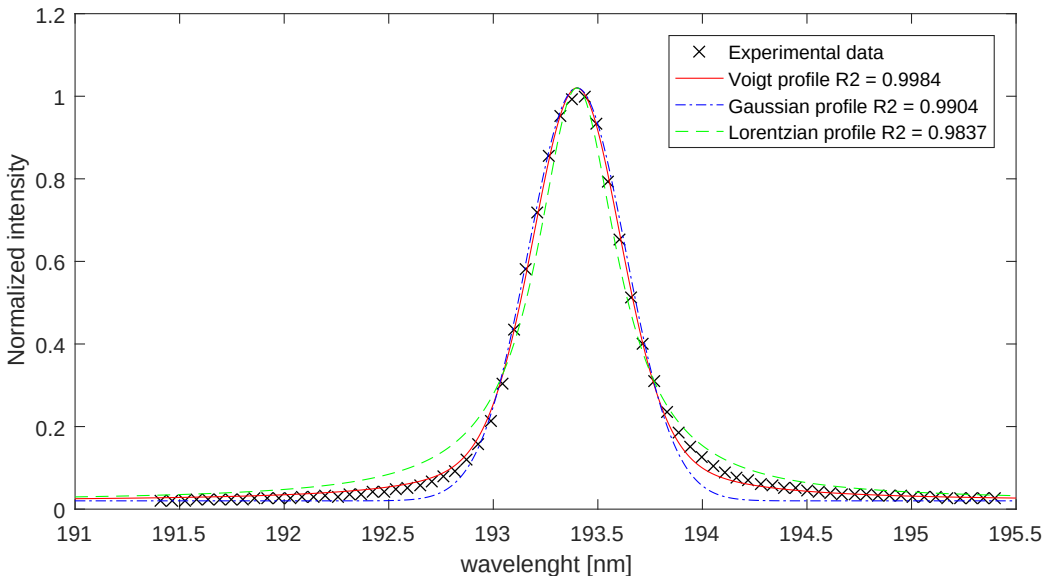

Fig. 1.3: comparison between Gausian, Lorentzian and pseudo-Voigt profile interpolation within the data of carbon emission line measured by LIBS technique

because it takes place due to interactions of the emitting atoms. A special case of this kind of broadening, which is very significant in the plasma spectroscopy, is the Stark broadening that occurs when the charged particles like ions collide each other. According to the general name of these broadenings, they have the Lorentzian distribution. There are more mechanisms of spectral line broadening like natural or Inhomogeneous broadening but they are negligible in plasma spectroscopy in comparison with others, described above.

We discussed above that the spectral line broadening mechanism has either Gaussian or Lorentzian distribution. Therefore, the resultant theoretical shape of an emission line must be something between of them. Mathematically, the resultant profile is the convolution of each broadening mechanism. This is a Voight profile that is defined as the convolution of Gaussian and Lorentzian distribution. In practise, we use the approximation called pseudo-Voigt profile, which uses the linear combination instead of the convolution and hence it is easier for implementation to the scripts of data processing. A comparison between Gausian, Lorentzian and pseudo-Voigt profile interpolation within the data of a carbon emission line measured by LIBS technique is shown in Fig 1.3

The analytical form of pseudo-Voigt function can be written as [31]

$$I_p(x) = I_p\{\eta C(x) + (1-\eta)G(x)\}, \tag{1.6}$$

where I_p is amplitude of the function and η is a Cauchy content (sometimes called as mixing coefficient). $C(x)$ is a Cauchy function (also known as Lorentzian function):

$$C(x) = \frac{1}{1+x^2}, \tag{1.7}$$

and $G(x)$ is Gaussian function:

$$G(x) = exp[-(\ln 2)x^2]. \tag{1.8}$$

x is an variable which is defined by the equation

$$x = \frac{p_0 - p}{w/2}, \tag{1.9}$$

where p_0 is the position of the maximum, p is a variable of the position (usually wavelength) and w is a full width at half maximum (FWHM). It is obvious that η can take any value between 0 to 1. According to the equation (1.6), the function $I_p(x)$ becomes Gaussian and Lorentzian for $\eta = 0$ and $\eta = 1$, respectively.

1.2.4 An analysis of ferrous alloys by LIBS

LIBS analysis of steel and cast iron, especially determination of light elements such as carbon, sulphur, and phosphorus, has been always very complicated because of the high concentrations of iron in these alloys. The high concentration of iron causes excitation of dozens of hight-intensity emission lines of iron, which interfere with much weaker lines of the light elements and hence they cannot be detected. Experiments proved this theory since emission lines of carbon, sulphur or phosphorus in UV-VIS-NIR spectral range are hard (or even imposible) to be detected by LIBS [32]. Despite that, these lines can be detected in the vacuum ultraviolet (VUV) without significant interference of the iron emissions. VUV radiation makes the analysis possible but less straightforward, in comparison with the analysis in UV-VIS-NIR, due to the absorption of VUV by the air (see chapter 1.3.1).

An analysis of a solid steel by LIBS in the range of 178-300 nm

Most of research works related to light elements analysis in steel by LIBS have been done in the range of 178-300 nm because this range of wavelengths comprises most of the emissions of elements that must be analysed in steel. The most prominent lines are shown in Tab. 1.1. V. Sturm and R. Noll demonstrated the limit of detection better than 10 μg/g for every element in Tab. 1.1 by use of Paschen-Runge spectrometer with PMT detectors, all purged with argon. Particularly, such a limit of detection for carbon, sulphur, and phosphorus in steel was achieved for the first time [6].

We have already mentioned in chapter 1.1 that SD-OES is currently the most popular analytical method in metallurgy. This method was compared with LIBS

Tab. 1.1: List of the elements, wavelengths, Einstein coefficients of spontaneous emission A_{ki}, and energies E_k and E_i of the upper and the lower levels, respectively, of the observed lines apropriate for LIBS analysis in the range of 178-300 nm. Data were taken from [5] and NIST (National Institute of Standards and Technology) database.

Element	Ionization stage	Wavelength [nm]	E_n [eV]	E_i [eV]	A_{ki} [s^{-1}]
P	I	178.28	6.95	0	$2.14 \cdot 10^8$
S	I	180.73	6.86	0	$3.27 \cdot 10^8$
Si	I	184.82	6.72	0.01	$1.23 \cdot 10^8$
Fe	II	187.75	9.13	2.52	$8.2 \cdot 10^7$
C	I	193.09	7.68	1.26	$3.39 \cdot 10^8$
Cr	II	205.56	6.03	0	$1.22 \cdot 10^8$
Ni	II	231.60	6.39	1.04	$2.88 \cdot 10^8$
Cr	II	267.72	6.18	1.55	-
Fe	II	271.44	5.55	0.99	$5.7 \cdot 10^7$
Si	I	288.16	5.08	0.78	$2.17 \cdot 10^8$
Mn	II	293.31	5.40	1.17	$2.04 \cdot 10^8$

by Hemmerlin in 2001 when analysed low concentrations (< 100 μg/g) of C, N, S, and P in steel by use of a setup that comprised Paschen-Runge spectrometer and a chamber purged by argon. The setup was used for LIBS as well as SD-OES analysis. They found that SD-OES has three times better LOD than LIBS. However, the LOD better than 5 μg/g for C, P and S were achieved by LIBS for the first time [7].

LIBS combined with the laser-induced fluorescence can be used with benefit for steel analysis in order to get rid of the difficulties related to the absorption of the VUV and interference of iron emissions. Phosphorus with LOD estimated around 0.7 μg/g was analysed in open air using LIBS-LIF by Shen in 2009 [33]. More recently, carbon was also analysed in the open air by use of the fluorescence of carbon-nitrogen radicals forming in the plasma when interacting with nitrogen atoms in the atmosphere [34]. The CN radicals were stimulated by a laser with the wavelength of 421.6 nm and emitted 388.34 nm fluorescence which is not affected by any interference with the iron line. They achieved LOD of 130 μg/g and 390 μg/g in the air and pure nitrogen gas, respectively.

Hand-held metal spectroscopic devices are also widely discussed in the field of chemical analyses. The leader in this field of the area has been the X-ray fluorescence (XRF) method. Nevertheless, this method is unable to detect light elements and hence some metal alloys cannot be investigated properly. For instance, XRF is not appropriate for C, P, S analysis in steel or for the Si, Li, Be, Mg analysis in

aluminum alloys. Therefore, many hand-held analysers using LIBS have appeared on the market, recently [35].

An analysis of a solid steel by LIBS below 100 nm

Detection of the radiation under 100 nm is an extraordinarily difficult task because of the very significant absorption of this sort of wavelengths by the air. Furthermore, there is no transmissive optics working in such wavelengths. Therefore, only vacuum compatible Paschen-Runge spectrometer and specialised optical components such as glass capillary array [36] must be used in an experimental setup. The setup is then expensive but very good LOD for light elements in steel can be achieved. Kharter in 2000 measured LOD of 1.2 $\pm$0.2 μg/g for carbon in low alloy steel by use of C III 97.7 nm [37]. More recently, Jiang (2014) demonstrated the impact of the ambient atmosphere on the LOD of carbon and sulphur by use of the single-pulse technique as well as the double-pulse technique. They achieved the best performances with the nitrogen of the pressure of 0.3 mbar. The LOD for carbon and sulphur in steel was 2.9 μg/g and 1,5 μg/g, respectively. The calibration curve was done for the C III 97.7 nm and S V 78, 65 nm emission line, respectively.

An analysis of a molten steel

On-line analysis of a molten steel from the furnace has always been very attractive for metallurgist because it would reduce the cost and time needed for the analysis. LIBS has been the only method for such a remote analysis, so far, and hence many researches were devoted to this topic. Nevertheless, this is extremely technically challenging because of the absorption that we discussed above. Peter, Sturm, and Noll, however, [38] developed a device, which overcame this obstacle with LODs for C, P, and S of bellow 20 μg/g.

1.3 Ultraviolet radiation (UV)

The ultraviolet radiation is defined as an electromagnetic radiation from 100 nm to 400 nm. The Ultraviolet is further divided into Near Ultraviolet (NUV: 300-400 nm), Middle ultraviolet (MUV: 200-300 nm), Far Ultraviolet (FUV: 122-200 nm), Vacuum Ultraviolet (VUV: 10-200 nm), Extreme Ultraviolet (EUV: 10-121 nm), etc.

For the purposes of this thesis, the range of the wavelength under 200 nm is important. This range of wavelengths is not significantly absorbed only by particular gases, such as argon, helium, nitrogen etc., or a vacuum. Therefore it is often called as the Vacuum Ultraviolet (VUV).

1.3.1 Vacuum Ultraviolet (VUV) radiation in the air

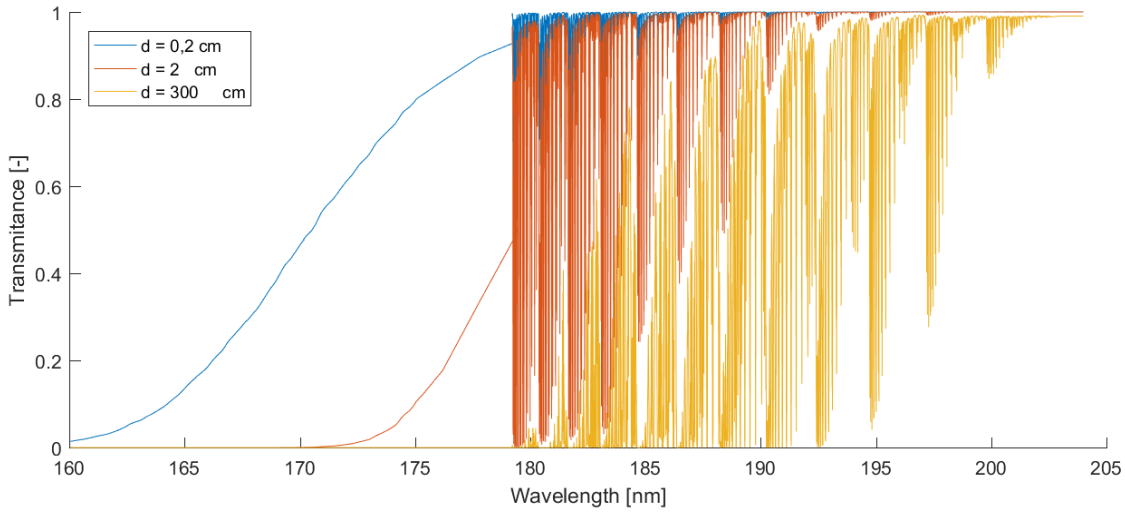

Fig. 1.4: The transmittance of the VUV passing through the oxygen with the temperature of 300 K, the pressure of 200 mbar and the absorption path length of 0.2, 2 and 300 cm

In order to outline the challenges related to the VUV detection, the absorption of the radiation under 250 nm has been investigated.

Absorption of a radiation coming through a certain material is determined by Beer-Lambert law which can be expressed as:

$$I = I_0 \mathrm{e}^{-\alpha(\lambda)d}, \tag{1.10}$$

where I_0 and I are the irradiations of the incident and the transmitted light, respectively and d is the absorption path length. $\alpha(\lambda)$ is the absorption coefficient given by

$$\alpha(\lambda) = \sigma(\lambda).n, \tag{1.11}$$

where $\sigma(\lambda)$ is absorption cross-section. It is experimentally determined constant, depending on the wavelength of the radiation, the chemical composition of absorption layer and temperature of the absorber. There is a website containing a database of this constant for a wide variety of absorbers and range of wavelengths [39]. In this work, we used especially a research published by Yoshino [40]. n is a concentration of the absorber, which can be determined by the equation of state given by

$$n = N_A \frac{pV}{RT}, \tag{1.12}$$

where $N_A = 6.022 \times 10^{23}$ mol^{-1} is Avogadro's constant and R is gas constant. p, V and T is partial pressure, volume and temperature of the absorber, respectively.

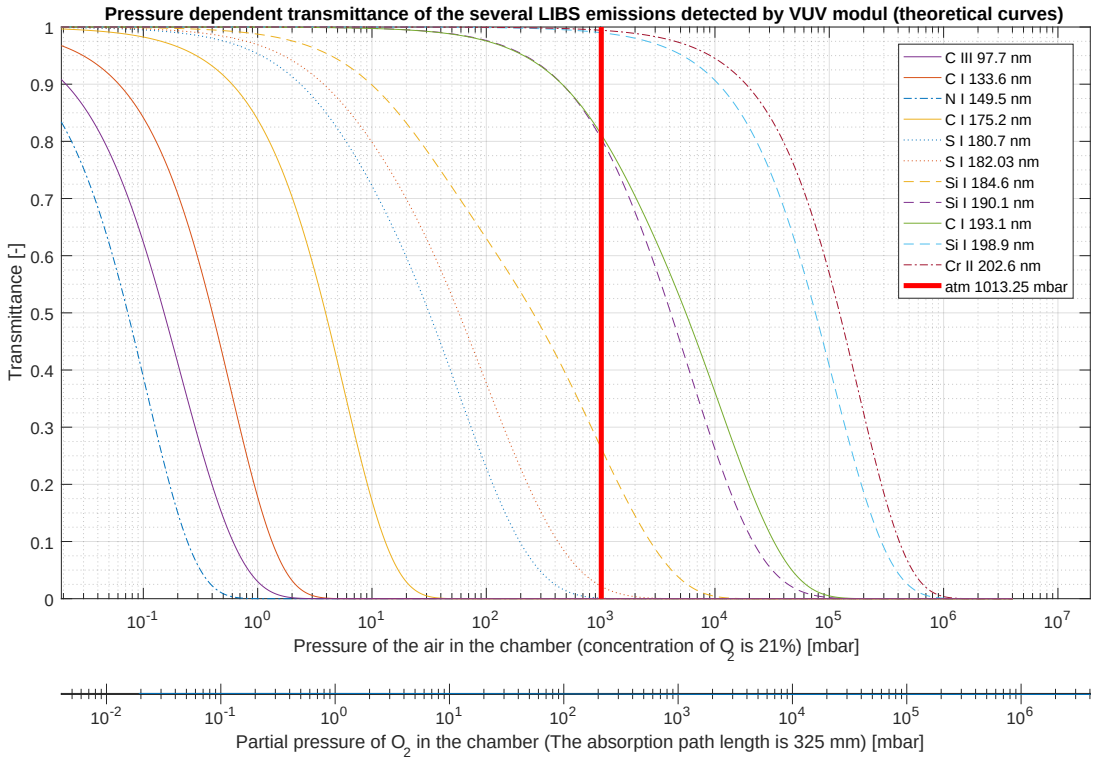

Fig. 1.5: The transmittance of the several LIBS emissions in VUV passing through the air

A dimension of the absorption cross section $\sigma(\lambda)$ is often declared in a unit of cm^2.(amount of molecules)$^{-1}$. Therefore the parameters in the equations (1.10) and (1.12) have to be set in the units of Kelvin, Pascal, cm^3 and cm for the temperature T, pressure p, volume V and path length d, respectively.

The degree of absorption can be shown by a transmittance defined as a ratio of the intensity of the transmitted light I_0 to the intensity of the incident light I:

$$T = \frac{I}{I_0} \tag{1.13}$$

The equations (1.10) and (1.13) yield the equation for transmittance in a gas:

$$T = e^{\sigma(\lambda)dn}. \tag{1.14}$$

The atmosphere of earth contains roughly 20 % O_2 and 80 % N_2. There are also small amount of other compounds including Ar, CO_2, H_2O, etc., but their contribution to the absorption is negligible. Furthermore, nitrogen is perfectly transparent for VUV, so that oxygen is the only element absorbing the VUV radiation. The transmittance of the radiation between 150 nm and 210 nm passing through oxygen with the temperature of 300 K, the pressure of 200 mbar and the absorption path

length of 0.2, 2 and 300 cm, respectively, is depicted in fig.1.4. The Shuman-Runge bands are plain to see in the range 175–200 nm. The Shuman-Runge continuum occurs in the range 130–175 nm and the range 200–242 nm is called Herzberg continuum.

A pressure-dependent transmittance of the most important LIBS emissions passing through the absorbing path length of 325 mm (this length has been estimated for further design of VUV module) is depicted in the Fig. 1.5. The tick values along the upper portion of the horizontal axis are evaluated for the partial pressure of O_2. The second horizontal axis shows the pressure of the air in the case that the concentration of oxygen in the air is 20%.

The vertical red line in Fig. 1.5 shows the border of atmospheric pressure of absorbing oxygen, which reveals that the wavelengths down to 190 nm are not significantly absorbed even in the atmospheric pressure. For instance, over 80 % of the C I 193.1 nm emission line is transmitted. The transmission declines sharply bellow 190 nm and almost no signal can be observed under 180 nm. For example, nearly 30 % of the Si 184.6 nm is still visible but the intensity of S I 182.03 nm is negligible. Therefore, If we want to detect a strong signal of the emission lines below 180 nm, which is crucial in a steel analysis, the partial pressure of oxygen in the whole optical path has to be reduced at least to the partial pressure of 10 mbar. The easiest way to do this is to purge the optical path by a gas transmitting VUV such as inert gases (Ar, He or N)[41].

1.3.2 Transmission of UV radiation by optical glasses

The glasses widely used in optics have a low transmittance of ultraviolet radiation. The flint and crown glasses containing SiO_2, and other ingredients, absorb all wavelengths under 300 nm. Only the high pure glass of SiO_2 called fused quartz or fused silica has a good transmittance in UV. The absorption starts to be significant under 150 nm. Other special optical materials transmitting VUV are crystals, which have many applications in coatings and thin layers. Particularly, CaF_2 and MgF_2 are appropriate for the wavelengths down to 120 nm. On the other hand, crystals are not as hard and thermally stable as traditional optical glasses. [42]

Although the quartz has good transmittance for VUV in general, the manufacturers do not recommend the use of optical fibres, based on the quartz, for UV radiation. Standard optical fibres are progressively damaged by radiation under 230 nm and their transmittance decreasing due to solarization effect. Though the manufacturers developed solarization resistant fibers for Deep UV applications, their transmittance is not appropriate for LIBS in long-term use.

The specific discipline is a work with the wavelengths under 100 nm because

there is no material transmitting these wavelengths so that only reflected optical components must be used. However, many experiments and devices require at least the separation of different pressure regions. For instance, concerning particular LIBS application [10], the plasma must be excited in ambient inert gas while its UV radiation is detected in VUV spectrometer operating in the ultra-high vacuum (UHV). This divider can be designed in the form of either thin-film windows, differentially pumped slits or more recently, capillary array [36]. Even, lens focusing extremely deep ultraviolet or X-ray has been developed based on diffraction and Fresnel zones approach. This sort of lens is called zone plate because it is basically a plate with dark and bright zones. Since the dark zones absorb the radiation, the zone plates have low-efficiency [43].

1.4 Data processing/Chemometrics

The main purposes of a spectroscopy are concerned with qualitative or quantitative determination of sample chemical composition. Apparently, this sort of information, especially concerning quantitative analysis, cannot be determined directly from the raw data given by the spectrometer in a form of the light spectrum. Statistics must be taken into account in order to separate just a useful and clear result such as the proportional concentration of the respective element in the sample.

The spectrometer output (the spectrum) is a vector of intensities I corresponding to respective pixel/detector and integrated over the exposure time (gate width) t_{int}. The value of the pixel can be then converted to the wavelength (see chapter 3.1.1).

Assuming an experiment that comprises m amount of spectra (measurements/observations) and a detector with p pixels (variables), we can mathematically express the experiment in the form of a matrix as follows:

$$\mathbf{X} = \begin{bmatrix} I_{11} & I_{12} & \dots & I_{1p} \\ I_{21} & I_{22} & \dots & I_{2p} \\ \vdots & \vdots & \ddots & \vdots \\ I_{m1} & I_{m2} & \dots & I_{mp} \end{bmatrix} \tag{1.15}$$

Individual rows of the matrix $\mathbf{X}$ represent either the whole spectrum or a part of the spectrum in the vicinity of the emission line of the investigated element.

1.4.1 Data pretreatment

The spectrum is dependent upon the measuring conditions, which can vary during the measurement. Particularly, the LIBS deals with the fluctuation of the laser energy. Other fluctuations of the intensities among the spectrum can be caused by

the inhomogeneous microstructure of the sample, ambient atmosphere and so on. Therefore, the data normalization is recommended for every quantitative analysis.

The data normalization means that the intensities of the matrix $\mathbf{X}$ (1.15) are divided by a reference intensity $\mathbf{I_r}$ [6] :

$$\mathbf{X_N} = \mathbf{X}./\mathbf{I_r}, \tag{1.16}$$

where the reference intensity is determined for every measurement individually:

$$\mathbf{I_r} = \begin{bmatrix} I_{r1} \\ I_{r2} \\ \vdots \\ I_{rm} \end{bmatrix} \tag{1.17}$$

There are many approaches for determination of the reference intensity. The straightforward strategy is to compute the reference intensity as the intensity of the whole spectrum or as the maximum spectral peak intensity. A more convenient approach, however, is so-called internal standardization, meaning that the reference intensity is the intensity of an emission line corresponding to the matrix element with known concentration. The internal standardization achieves, in general, better results but the proper emission line for standardization must be carefully chosen.

1.4.2 Calibration and limit of detection

Leaving aside the calibration-free methods of LIBS [44], the calibration must be applied in order to determine the chemical composition of unknowns. This approach comprises the measurement of several standard samples with the known chemical composition which should be also similar to the unknown sample because of the matrix effect. For every investigated element, the curve of growth (also known as calibration curve) is created as an interpolation within a set of points whose X and Y coordinates correspond to the known concentration of the respective element and to the measured intensity of the matching emission line, respectively. The shape of the interpolation is ideally linear. Nevertheless, the mechanism such as self-absorption of emission lines causes non-linearity of the curve of growth[44].

The important parameter of a spectroscopic device or a method are the Limit of Detection (LOD) for an investigated element. LOD is the smallest possible concentration of an element in the sample that can be measured with statistical certainty. The equation frequently used for LOD evaluation is:

$$LOD = k.\left(\frac{s_b}{X_b}\right)\left(\frac{X_b}{b}\right) \tag{1.18}$$

[6] ./ is the operator for element-wise right-array division. In the case of the equation (1.15), it means that every row of the matrix $\mathbf{X}$ is divided by the matching intensity from the matrix $\mathbf{I_r}$.

where s_b is the standard deviation of either the background of the blank or the sample with the smallest concentration. X_b is the mean of the background or the blank and b is the slope of the linear part of the calibration curve. The last coefficient is frequently chosen as $k = 3$ (1.18). The expression in the first parenthesis (s_b/X_b) is the Relative Standard Deviation (RSD) and the expression in the second parenthesis (X_b/b) determines Background Equivalent Concentration (BEC).

The equation (1.18) is in conformity with the recommendation of International Union of Pure and Applied Chemistry (IUPAC) [45] and it has been also suggested for LIBS technique by Hahn [44].

1.4.3 Principal Component Analysis (PCA)

Principal Component Analysis (PCA) is a linear multivariate analysis that aims to extract only the most crucial information of the dataset $\mathbf{X}$ and order them into new variables called principal components. The PCA is capable of visualizing the pattern of similarities among the measurements and to determine the importance/weights of individual variables. Therefore, the PCA is good tool for preliminary analysis of the studied dataset or for the classification of the dataset.

The PCA yields matrices containing principals components in such a way as a linear combination of these matrices is equal to the original dataset:

$$\mathbf{X} = \mathbf{F}\mathbf{Q}^T, \tag{1.19}$$

where $\mathbf{F}$ and $\mathbf{Q}$ is called a Score and a Loading, respectively. The Loading is a vector of directions defining a model of the dataset. The Score is a projection of the dataset observations to these vectors of the Loading. Hence, Score matrix reveals the pattern of similarities among the observations since it makes clusters of points in the PC space. For instance, Fig. 5.6 shows the scores plot of five steel samples represented by individual LIBS measurements, which are distinguished in PC space by individual clusters. In terms of the use of PCA to a spectroscopic data, the Loading shows, which wavelengths are responsible for the extraordinary position of respective cluster. Fig. 5.5 shows matching Loadings to the scores in Fig. 5.6. One can see that Fe, C, and Cr are responsible for the extraordinary positions of the clusters in PC1 direction because the emission lines of those elements are extraordinarily intense. The positions of clusters in PC2 are made up rather by C and Cr and the third direction of PC3 is represented rather only by C. This behavior of PCA is convenient for the classification because different samples are well distinguished by Score and their chemical composition can be estimated by Loading.

The power of the PCA is that the dimension of the data is significantly reduced while useful information remains because only a few most essential components

(typically from 3 to 10 PC's), usually containing more than 99% of the information, are separated and used for further analysis. This technique combined with other methods like SIMCA is very useful in autonomous classification of samples. Further applications of PCA concerning LIBS technique have also been found in chemical mapping [46, 47] or spectral outlier filtering [48]. More information and mathematical principles of PCA can be found in [49, 50, 51].

2 The optical design and the concept of VUV module

2.1 Assignment/Specification

The work of this thesis aims to develop a module for detection of the radiation down to 178 nm and implement this module to the experimental LIBS setup of the Laboratory of laser spectroscopy in Brno. The capability of the module will be demonstrated by the LIBS analysis of several steel samples. The main requirements are summarised as follows:

- The module is equipped with the flange F58, which is mounted in the B type port of the interaction chamber. See the chapter 2.2 describing the properties of the interaction chamber.
- The module is vacuum tight (The lowest possible pressure in the chamber is 1 mbar). Furthermore, the module offers a purging of the optical path by an inert gas in order to reduce the absorption of the VUV radiation by the air.
- The radiation of the plasma is collected and imaged on the slit of the spectrometer by collection optics placed inside the chamber. Either Solar FA-2 objective or the objective comprised two CaF_2 lenses will be used (see chapter 2.4).
- Ibsen HR-DUV spectrometer with the spectral range of 178 to 409 nm is used.
- A kinematic mounting of either spectrometer or the collection optic offers both, the fine positioning perpendicular to the optical axis in both directions (X and Y), as well as coarse positioning parallel to the optical axis.
- The fine adjustment of X and Y positioning provides at least the travel of $\pm$ 1 mm. The coarse positioning of Z-direction offers at least the travel of $\pm$ 5 mm. The accuracy, as well as the resolution of the Z positioning, is not crucial, but its rigidity should be hight.
- The manual adjustment has to be easily accessible from the outside of the chamber.
- A distance between the plasma and the input port of the flange is, approximately, 132 mm (see Fig 3.1)
- The spectrometer is easily removable and the holder of the spectrometer provides the mounting of the fibre, that is connected to the laser, for coarse adjustment of the optical system.

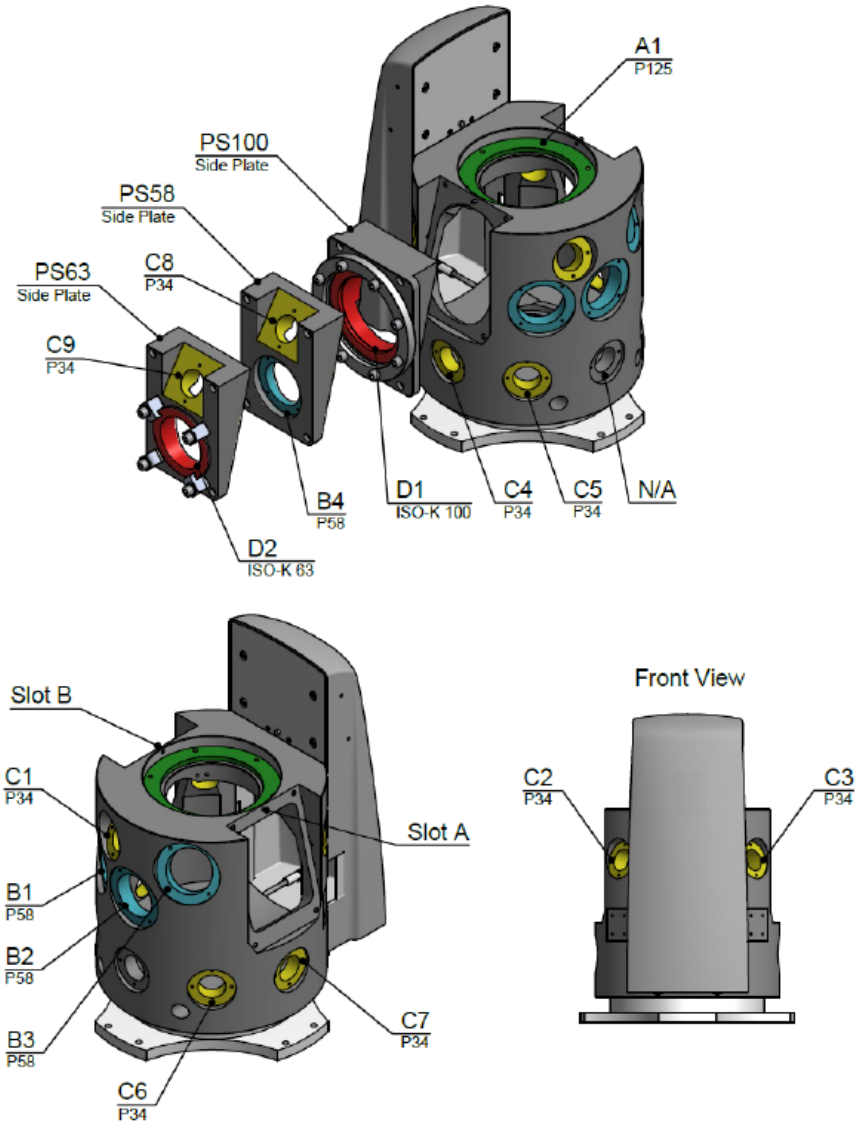

Fig. 2.1: Ports and side plates of the interaction chamber

2.2 Interaction chamber

The interaction chamber is the basic component of the LIBS setup of the Laboratory of laser spectroscopy in Brno because it associates all modules needed for the analysis. A deep understanding of all functionalities of the chamber is necessary for further development of the module in this thesis.

Precise 3-axis vacuum-compatible motorized manipulator holding the sample is placed in the centre of the chamber. The appropriate area of the sample is found by the movement in both the X and the Y axis, which also enable the mapping of the sample surface that is necessary for the reconstruction of the sample overview and for the chemical mapping. The sample surface is placed in the proper position,

where the laser beam is focused, by the movement in the Z-axis.

The chamber is equipped with ports schematically depicted in Fig. 2.1 including:

- **A1 port** (green) is reserved for primary input module, which provides with two functionalities of the LIBS system. First, it captures the surface of the sample, which is important for both the sample overview and for proper focusing of the sample surface [52]. Second, the laser beam is introduced into the chamber by this module and focused on the surface of the sample by a focusing lens. The focusing lens is mounted in a motorized translation stage and thus the spot-size of the laser beam on the sample surface can be changed. The clear aperture of the A port is 125 mm.
- **B ports** (blue) are very suitable for collection optics and secondary cameras because their geometrical axis intersects the center of the chamber. The clear aperture of the B port is 58 mm.
- **C ports** (yellow) are used mainly for ancillary modules such as input and output of Pressure Regulation Module, Emergency Equalization, Sound Pressure Module, etc. The axis of C1, C2, C3, C8 and C9 ports are aimed towards the centre of the chamber but C4, C5, C6 and C7 are not. The clear aperture of the C port is 34 mm.
- **D ports** (red) is intended for the international standard flange ISO-K 100. This flange is primarily used as a viewport.

2.3 Collection optics

Most of the collection optics currently used in the Laboratory of laser spectroscopy in Brno rely on optical fibres. The scheme of the common collection system in both adjustment and measurement configuration is shown in upper and lower portion of Fig. 2.2, respectively. Once the ablation laser is adjusted to the centre of the chamber, clearly visible crater is ablated on the surface of the sample. This crater serves as the target for the adjustment of the collection optics that is proceeded as follows: A laser diode is connected to the optical fibre, so that approximately a point source of radiation is emitted from the output of the fibre. The output is then connected to the XYZ adjustable mounting that enables the pencil, passing through the collecting lens, to be focused precisely on the crater. Therefore, if the side of the fibre, that has been connected to the laser, is connected to the spectrometer and the plasma is induced on the sample by ablation laser, the plasma radiation is precisely collected to the optical fibre and introduced to the spectrometer.

This technique allows straightforward adjustment of the collection system but there are some drawbacks. We showed in chapter 1.3.1 that a standard optical fibres are not appropriate for wavelengths below 200 nm. Therefore this collection

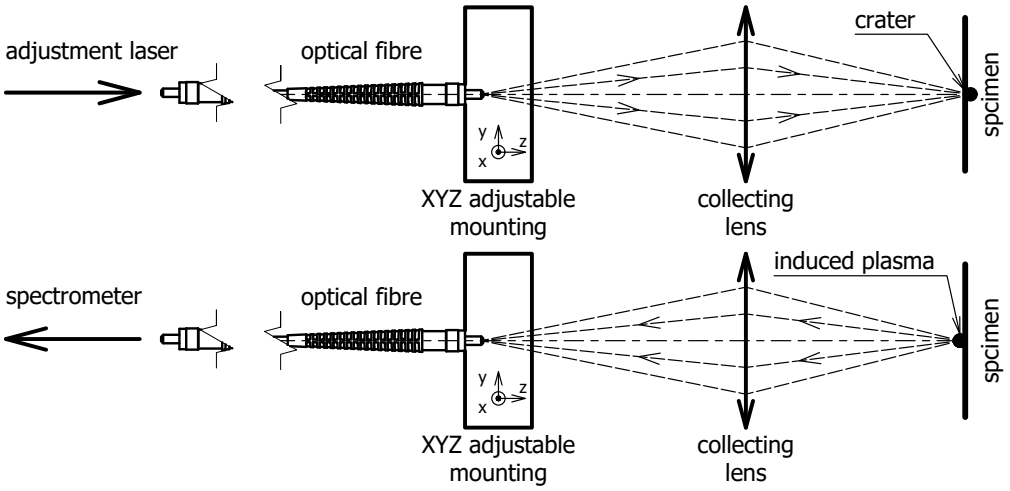

Fig. 2.2: Adjustment (upper) and measurement (bellow) configuration of current design

system is not appropriate for VUV radiation either. Moreover, the optical fibres have considerable attenuation even for UV-VIS-NIR, which can be a problem for some application in which the intensity of the plasma radiation is weak.

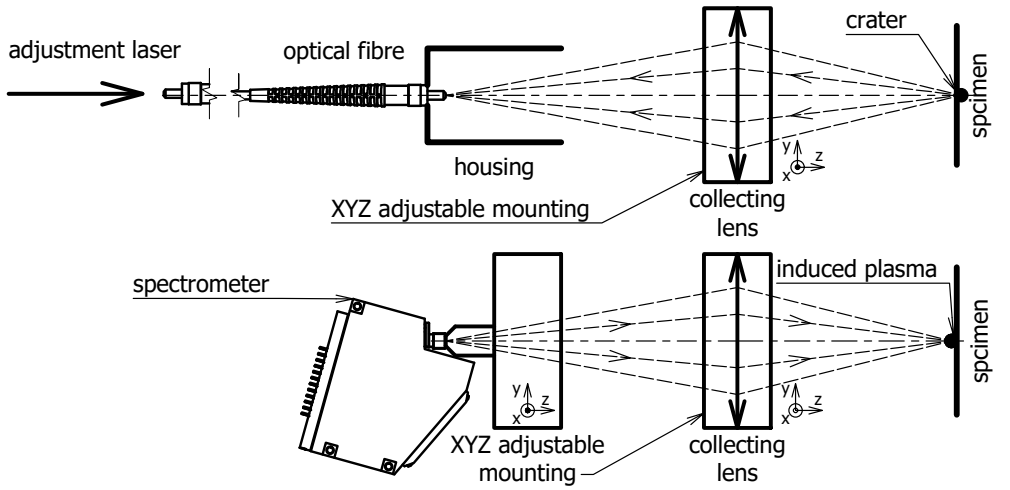

Fig. 2.3: Scheme of adjustment (upper) and measurement (bellow) of proposed design

Due to the attenuation of the fibres, the direct introduction of the VUV radiation from the plasma into the spectrometer is necessary. This is quite easy at first sight but it turns out to be challenging when we consider the adjustment of such a system. Proposed solution is showed in Fig. 2.3. During the adjustment (see upper portion of the Fig. 2.3), the laser diode is connected through the optical fibre to the housing that holds the fibre in proper position in respect to the a collection lens. The pencil

of laser radiation is focused on the flat surface of the specimen by the collecting lens, which is mounted in adjustable XYZ adjustable mounting. The lens is then moved by the mounting in order to target the pencil to the crater.

After this rough adjustment, the holder with the optical fibre is switched to a spectrometer (see lower portion of the Fig. 2.3) that is either mounted in an adjustable mounting or in a calibrated part that holds the slit of the spectrometer in approximately the same place as the position of the fibre pinhole during adjustment.

2.4 Optical design

The behavior of the optical systems has been investigated by the theory of paraxial ABCD matrices [42]. For our purpose, we will need transformation matrix for transition over the distance L:

$$\begin{bmatrix} 1 & L \\ 0 & 1 \end{bmatrix} \tag{2.1}$$

and for refraction at an interface with changing refractive indices $n \to n'$ and radius of curvature r :

$$\begin{bmatrix} 1 & 0 \\ \frac{n-n'}{n'r} & \frac{n}{n'} \end{bmatrix} \tag{2.2}$$

2.4.1 Collection optic consisted of two plan-convex lenses

The transformation matrix of the optical system consisted of two plan-convex lenses (see Fig. 2.4) in the air ($n \approx 1$) made up by the matrices above can be expressed as:

$$M = \begin{bmatrix} A & B \\ C & D \end{bmatrix} = \begin{bmatrix} 1 & 0 \\ 0 & n \end{bmatrix} \begin{bmatrix} 1 & t \\ 0 & 1 \end{bmatrix} \begin{bmatrix} 1 & 0 \\ \frac{1-n}{nR} & \frac{1}{n} \end{bmatrix} \begin{bmatrix} 1 & d \\ 0 & 1 \end{bmatrix} \begin{bmatrix} 1 & 0 \\ \frac{n-1}{-R} & n \end{bmatrix} \begin{bmatrix} 1 & t \\ 0 & 1 \end{bmatrix} \begin{bmatrix} 1 & 0 \\ 0 & \frac{1}{n} \end{bmatrix} \tag{2.3}$$

where A, B, C and D are coefficients defining the paraxial optical system and n is the refractive index of both lenses. The intersection length of a paraxial ray in the image space s' can be expressed from these coefficients as: [42]

$$s' = \frac{sA - B}{D - sC} \tag{2.4}$$

The optical system will operate in a broad range of wavelengths from 178 nm to 400 nm. Therefore, one would expect very significant chromatic aberration since refractive index rapidly changes in ultraviolet. Conveniently, refractive index is expressed by use of Sellmeier equation given by [53]

$$n(\lambda) = \sqrt{1 + \sum_{i=1}^{M} A_i \frac{\lambda^2}{\lambda^2 - \lambda_i^2}}, \tag{2.5}$$

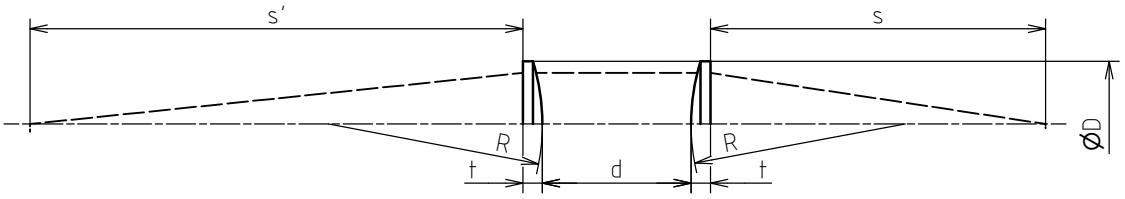

Fig. 2.4: Scheme of the optical path comprised by two plan-convex lenses

where both A_i (sometimes B_i) and λ_i (or C_i) are the Sellmeier coefficients, and λ is wavelength of the refracted light. The Sellmeier coefficients for CaF_2 have been taken from [54].

The f-number (i.e. $f_{\#} = \frac{f}{D}$, where f is the focal length and D is the diameter of the entrance pupil) of the optical system should be as low as possible in order to collect as much light as can be. It means that the lens must be near the plasma and its diameter has to be as large as possible. There is, however, a limitation in the distance between the first lens of the optical system and the sample due to the collisions of other devices inside the chamber. This distance depends also on the diameter of the system. For instance, it cannot fall below 60 mm for the 1 inch (25.4 mm) lens in diameter. Further requirement is concerned with the overall distance between the plasma and the entrance slit of the spectrometer. This length should be approximately 220 mm.

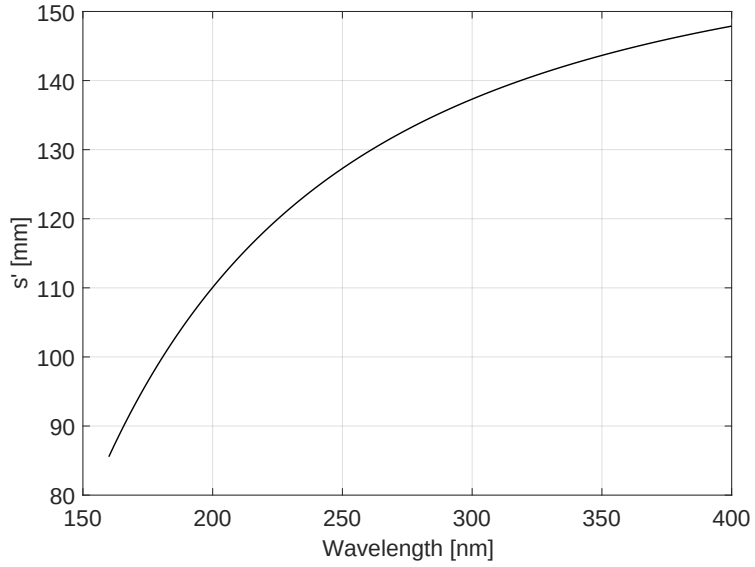

Fig. 2.5: Dependence of the intersection length of a paraxial ray in the image space s' to the wavelength λ

According to that specifications, two plano-convex CaF_2 lenses with the focal

length (at $\lambda = 588$ nm) and the diameter of $f = 100$ mm and $D = 25.4$ mm, respectively, were proposed. The gap between the lenses is $d = 30.2$ mm and the distance between the light source (plasma excitation) and the first lens is $s = 68$ mm. The radius of curvature of the lens's surface is $R = 43.4$ mm and the center thickness of the lens is $t = 3.9$ mm. All design parameters are schematically depicted in Fig. 2.4

The intersection length of a paraxial ray in the image space s' for the wavelengths between 150 to 400 nm computed by the equations (2.3), (2.4) and (2.5) is shown in Fig. 2.5. One can see very significant chromatic aberration of this system; the difference of the image position for 178 and 400 nm is more than 50 mm. Such an unexpectedly large chromatic aberration is caused by the fact that refractive index of the light changes in ultraviolet much more rapidly than in the visible region.

2.4.2 Two-lens achromatic objective

The second collection optic with correction of chromatic aberration has been proposed. It comprises a two-lens achromatic objective demounted from the achromatic Fiber Adapter FA-2 (SOLAR Laser Systems). The diameter is 15 mm and the focal length is 44.5 mm. The manufacturer was not able to provide us neither with the information about the aberrations of this system nor with the geometry of the lenses inside the objective. Therefore, both collection optics will be compared only experimentally in chapter 3.1.3.

In order to compute the intersection length of a paraxial ray in the image space s' of this optical system defined only by its focal length f', the lens maker's formula was used:

$$s' = \frac{sf'}{s + f'}. \tag{2.6}$$

3 The design of VUV module

3.1 Experimental module

The experimental module was proposed in order to test the main concept of the VUV analysis prior to the development of the final iteration. The experimental module is the important part of the development of a new device because it can reveal hidden challenges and obstacles to the concept. This module aims to test the following features:

- Detection of VUV radiation passing through a variety of absorbing conditions and to compare the results with the theory discussed in the chapter 1.3.1.
- Test of the spectrometer Ibsen FREEDOM HR-DUV, meaning to check the right calibration, its repetition rate and its capability of detection in VUV.
- Comparison of two collection optics comprised CaF_2 lenses and commercial UV objective lens FA-2 (Solar).
- To find out the best strategy for adjusting the collection system and to decide whether the lens, the spectrometer or both of them should be adjustable.

The experimental module (see Fig. 3.1) relies mainly on the commercial optomechanics in order to maximally reduce its cost. The module is built on the standard flange F58 (1) holding the 30 mm cage system (Thorlabs) that comprises rods (2) with a diameter of 6 mm. The spectrometer (3) is placed outside the chamber and it is connected to the cage system through a holder (4) and Translation Mount (5)(Thorlabs), which enables the spectrometer to be finely adjusted in X as well as Y axis. Since the mount (5) is guided by the rods (2), the spectrometer can be roughly adjusted in Z axis by moving with the mount (5) along the rods (2). Holder (4) is also equipped with push-in fitting (6) that serve as the input of argon that has been chosen as the purging gas. The whole mechanism is airtight by virtue of a flange (7) and a shaft (8) that is sealed with an O-ring (9). The output hole for the purging gas is drilled in the upper part of the standard flange F58 (1) because the argon is heavier than the air and thus it will be pushed out of the module by the argon.

The collection lens (10) is mounted in the same type of the Translation Mount (5) as the spectrometer. Therefore, the XYZ adjustment of the lens relies on the same principles as the adjustment of the spectrometer. In the Fig. 3.1, the first of two lenses, i.e. the objective lens comprised CaF_2 lenses (11), is depicted. The second compared lens, i.e. commercial FA-2 (Solar) objective lens, is mounted in the Translation Mount (5) similarly.

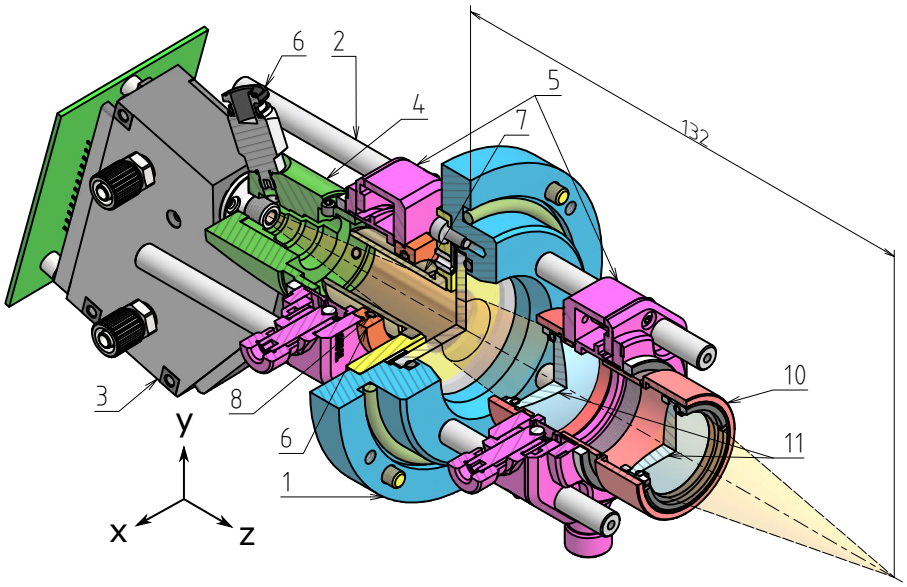

Fig. 3.1: Experimental module. 1 - Standard flange, 2 - Rods, 3 - Spectrometer Ibsen FREEDOM HR-DUV, 4 - Holder, 5 - Translation Mount, 6 - push-in fitting, 7 - flange, 8 - shaft, 9 - O-ring, 10 - Collecting Lens, 11 - CaF_2 lens.

3.1.1 Calibration of the spectrometer

The calibration of the spectrometer has been done by using the Mercury-Argon calibration lamp connected to the spectrometer through an optical fiber. The spectrum with labeled emissions of Hg is depicted in the Fig. 3.2.

According to the recognized emission lines of Hg, the proper wavelength $\lambda(pix)$ of any pixel of the detector can be determined by the calibration polynomial as follows:

$$\lambda(pix) = B_0 + B_1 \times pix + B_2 \times pix^2 + \cdots + B_n \times pix^n, \tag{3.1}$$

where B_0 stands for minimal wavelength, $B_1,\ B_2, \cdots,\ B_n$ are the calibration coefficients and pix is number of a pixel.

3.1.2 Test of the VUV absorption

The test of the absorption of the VUV radiation, passing through both the air and absorbing optical glasses, has been done by using the experimental module mounted in the interaction chamber. Among the first portion of the test, The chamber, as well as the whole space in the module, where filled by the air with atmospheric pressure, and the sample was scanned by LIBS using a map of size 5 mm $\times$ 5 mm with 25 points and 5 shots per point. The grey curve in Fig. 3.3 shows the sum over those 125 spectra.

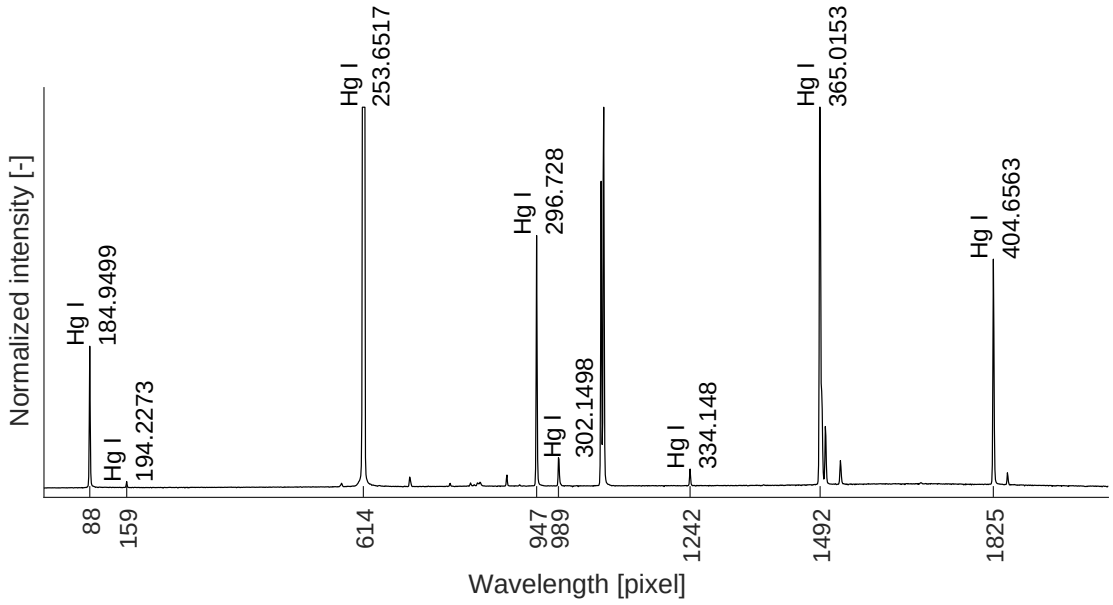

Fig. 3.2: The spectrum of the calibration lamp mercury Hg. The labelled lines have been used for evaluation of the calibration polynom.

In the second part of this test, the chamber was purged by argon and the same measurement was done. The result is depicted in Fig. 3.3 by the pink curve, which has higher values of intensities than the previous one. This enhancement is not caused by the reduction of absorbing air in the chamber but rather by the argon, which enhances the excitation.

In the last measurement, the whole optical path between the plasma and the detector was purged by argon (see the purple spectrum in Fig. 3.3). This signal can be considered as a spectrum of unabsorbed radiation from the plasma. The signal is approximately the same as the previous signal for wavelength bigger than 190 nm. The absorption of the previous measurement signal grows enough to be clearly observable in this absorbing conditions under the wavelength of 190 nm. Eventually, there is no signal under 180 nm although the peak around 178 nm has been exited as shows the unabsorbed (purple) spectrum. Similar behavior of the absorption has been theoretically predicted in chapter 1.3.1.

3.1.3 Test of the optical design

Both, the doublet comprising two CaF_2 lenses and the achromatic objective FA-2, were experientially tested by LIBS measurement. The optics collected the plasma radiation onto the slit of the spectrometer and intensities in the spectrum were compared.

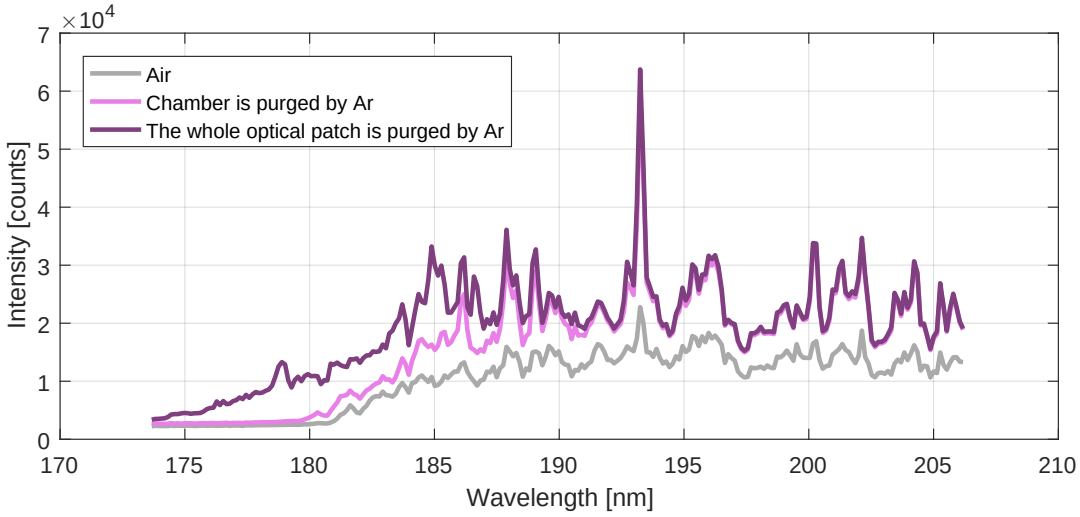

Fig. 3.3: LIBS spectrum in a different absorbing conditions. The grey one was measured in the air. The pink one was measured in the chamber purged by argon but with absorbing air in the spectrometer as well as in the optical path. The purple spectrum was measured in argon, purging whole optical path between the sample and detector

The doublet with two CaF_2 lenses was able to introduce more intense radiation into the spectrometer. However, the vicinity of the wavelength in the focus saturated the detector even for small pulse energy i.e., 1 mJ. On the other hand, the out-of-focus wavelengths in the boundary of the spectrum had small intensities due to the significant chromatic aberration of the optical system.

The plasma spectrum collected by the FA-2 was less intense but more uniform over the whole spectrum because the chromatic aberration of this objective was corrected. The saturation of the detector arose for much higher pulse energies i.e., approximately 40 mJ. A further advantage of the FA-2 is the small size in comparison with the second optics. Thus the implementation of the lens into the mechanics shall be easier. Therefore, the FA-2 achromatic objective is more appropriate for collection optics in VUV, even though the overall introduced radiation is less intense.

3.2 The final design

The second iteration (the final module) was proposed according to the feedback from the testing of the experimental module. The most crucial modifications for the second iteration are summarised as follows:

- The durability of the entire mechanism must be much higher
- Only collection lens shall be adjustable. The spectrometer can be stationary.
- The adjustment of the collection lens should be possible to control from the outside the chamber even in the case when there is a vacuum inside the chamber.
- The electronics of the spectrometer should be mounted in a holder.

3.2.1 Mechanism

In order to satisfy the requirements of the second iteration, the mechanism must have got rid of the standard optomechanical components. Thus the unique mechanism had to be designed. The simplified scheme of the principle of the movement in the X direction is shown in Fig. 3.4. The scheme shows two boundary positions of the mechanism in which the mechanism is eased (the left portion of Fig. 3.4) and maximally pressed down (the right portion of Fig. 3.4). One can distinguish four assemblies in Fig. 3.4, i.e. Master Translation Unit (MTU), Slave Translation Unit (STU), Horizontal Unit (HU) and Guided Unit (GU). The GU is the only assembly of the entire module that can move in all directions meaning in the X, the Y, and the Z. The two MTUs determine the position of the GU in the X and the Y. The two STUs press the GU against the MTUs, which enable the GU to move also in the reverse direction. The same principle of the mechanism is used in the Y axis, meaning the displacement of the direction perpendicular to the X. The HU provides the displacement in Z since the shaft (11) moves with the slider (8) along the Z. The overview of the entire module including all parts is schematically depicted in the Fig. 3.5. All units (i.e., MTU, STU, HU, and GU) are assembled in a Main Block (1) and a Flange (2) which can be mounted in the B port of the interaction chamber.

Master Translation Unit (see the left-bottom portion of the Fig. 3.5) relies on a wedge mechanism consisted of a Linear slider (3M) touching Bearing Balls (4M) that steer a wedge (5M) in X (or Y) direction while the Linear slider (3M) is pushed by an Adjustment Screw (6). The Wedge (5M) is also pressed against a fixed Housing (7M) by two springs (S_1) symmetrically and one spring (S_2) at the axis of the symmetry due to the kinetics of the mechanism, which was optimized in the dynamic simulation described in chapter 3.2.2.

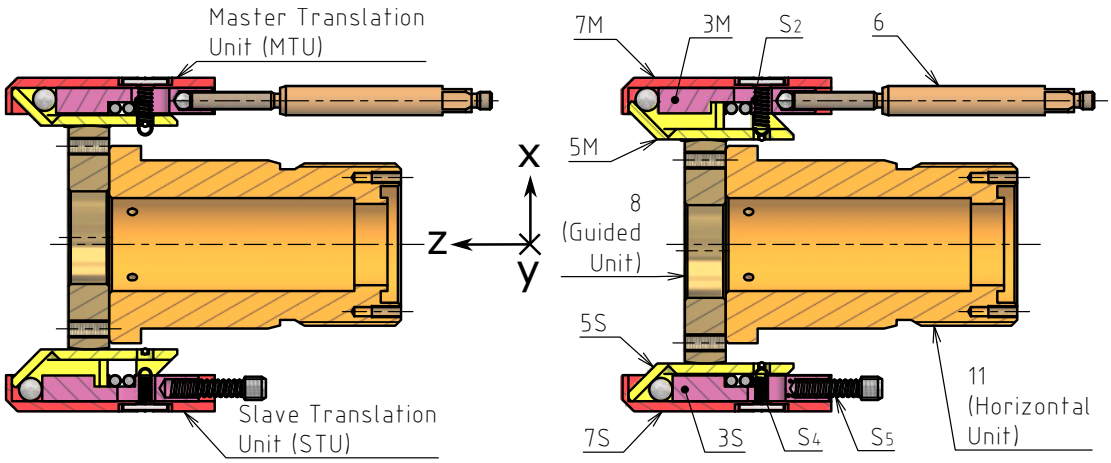

Fig. 3.4: Principle of the mechanism (only the X displacement): 3M/3S - Wedge Block of Master Translation Unit (MTU)/Slave Translation Unit (STU); 4M/4S - Bearing balls of MTU/STU; 5M/5S - Wedge of MTU/STU; 6 - Adjustment Screw; 7M/7S - Housing of MTU/STU; 11 - Shaft; S_2, S_4 - Springs. The left and the right portion shows the eased and pressed mechanism, respectively

Slider (8) which is assembled with a Lens Mounting (9) and the Lens (10) is the main component of the Guided Unit. The whole unit is pushed against a flat surface of a Shaft (11) by four springs (S_3) that fixes the block horizontally but not vertically. Thus, the slider can be finely adjusted to any vertical position (X, Y) by the two Master Translation Units placed perpendicularly each other. Adjustment in the horizontal Z direction is provided by a linear motion of the shaft (11) which makes up the Horizontal Unit (HU). The shaft (11) is mounted in the slide bearing that is part of the flange (2) and its fine positioning is enabled by a Union Nut (12). Obviously, the rotation of the shaft (11) must be secured. Otherwise the shaft would turn together with the union nut (12). This relative rotation between the shaft (11) and the flange (2) is prevented by a key (it is not visible in the Fig. 3.5) that is guided in a keyseat milled in the shaft. The key is screwed in the keyway of the flange (2).

The Slave Translation Unit (STU) comprises exactly the same machined parts as Master Translation Unit (MTU). Only springs of that are different. One very weak spring (S_1) is at the centre and three compression springs (S_5) press the Wedge (5S) with a help from the other parts of the mechanism against Slider (8). Therefore, the Slider (8) is able to move in any direction because it is continuously pressed against Master Translation Unit in both X and Y axis by STU.

The shaft (11) as well as adjusting screws (6) must be sealed in order to achieve vacuum tightness of the module. The minimal pressure inside the chamber shall be down to 0.1 mbar. The shaft is sealed by an O-ring in the slide bearing of the

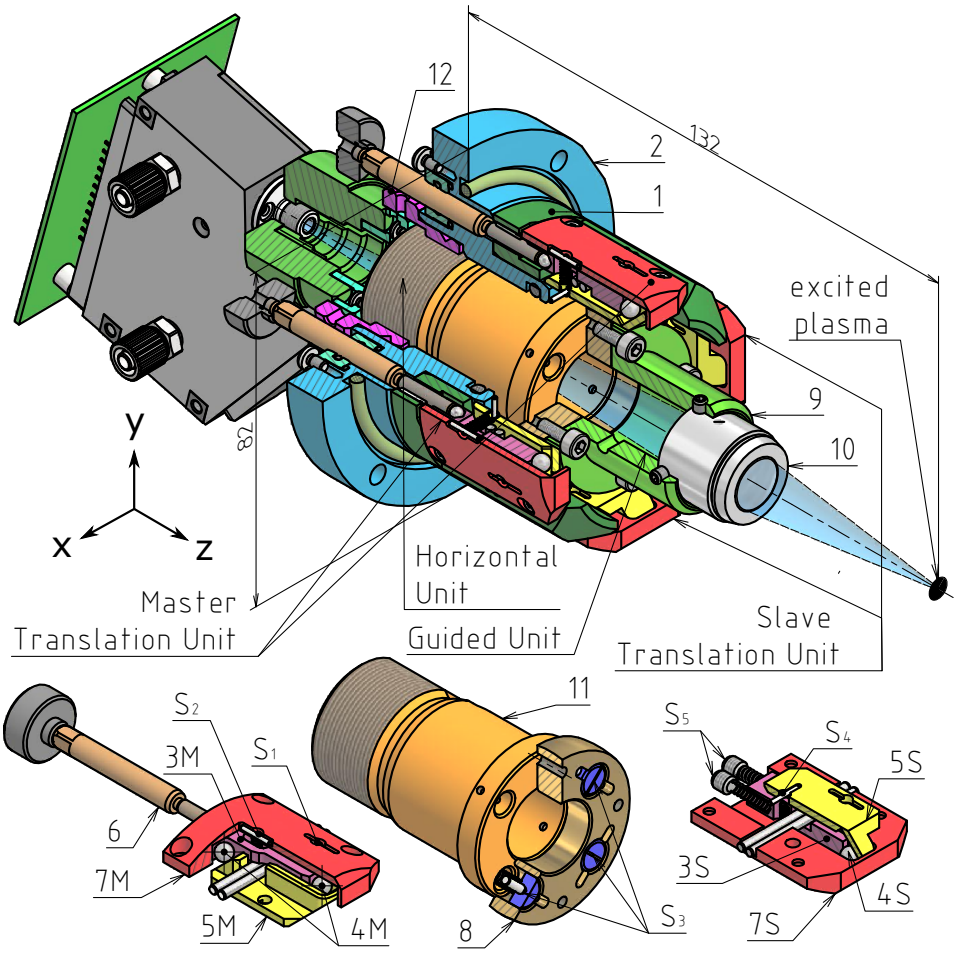

Fig. 3.5: Visualization of the mechanism: 1 - Main Block; 2 - Flange; 3M/3S - Wedge Block of Master Translation Unit (MTU)/Slave Translation Unit (STU); 4M/4S - Bearing balls of MTU/STU; 5M/5S - Wedge of MTU/STU; 6 - Adjustment Screw; 8M/8S - Housing of MTU/STU; 9 - Lens Mounting; 10 - Lens; 11 - Shaft; 12 - Union Nut; S_1, S_2, S_3, S_4 S_5 - Springs.

flange (2) guiding the shaft. The adjusting screw could not be sealed the same way because such a small groove for O-ring was impossible to manufacture. Therefore a housing that guides and seals the adjusting screw was proposed.

3.2.2 MSC ADAMS simulation of Master Translation Unit (MTU) and Slave Translation Unit (STU)

The kinematics of the mechanism was simulated in the MSC ADAMS in order to examine the proper work of the mechanism. The geometry of the mechanism of the entire VUV module was imported into the MSC ADAMS and the contacts between the parts were defined in the MSC ADAMS interface according to the manual.

The important task of the dynamic simulation was to investigate the forces in the contacts of MTU and STU and check out their magnitude. These forces were investigated in five different positions of the mechanism i.e. when the displacement of the guided unit is -1.2 mm, 0 and +1.2 mm in x direction and -5 mm, 0 and 5 mm in Z direction. In each position separately, the displacement in Y axis of the mechanism was driven and the forces of some contacts were recorded during the simulation. Fig. A.1 shows the distance-time graph of the simulation. The simulation started when the displacement of Y was -1.2 mm, meaning that the MTU, as well as STU of Y axis, were eased. Consequently, the displacement of Y started to increase in time across the curve determined by the cubic polynomial that has the relative maximum and minimum when the displacement of Y is maximal and minimal, respectively. In the maximal position that was reached in 2.4 seconds after the beginning of the simulation, the mechanism stopped for 0.5 s and then the displacement started to decrease with the same trend. This shape of the time-graph enabled smooth accelerating and decelerating of the mechanism because both the first and second derivation of the cubic polynomial is also continuous.

Fig. A.2, Fig. A.3, and Fig. A.4 show the forces in the contacts between the Wedge and the three balls (i.e., 4M position in the Fig. 3.5). The ↑ and ↓ show increasing and decreasing displacement, respectively, which have not the same propagation due to the friction in the mechanism. Similarly, Fig. A.6, Fig. A.7 and Fig. A.8 show the forces in STU. The main studied aspect of the trends depicted in those Figures was a minimal possible magnitude of the force. The higher the minimal possible magnitude, the more reliable the mechanism, because if the force in a contact were near zero (or even negative), the contact would become non-functional and thus the mechanism shall not work properly. On the other hand, the higher the minimal possible magnitude, the less accuracy of the mechanism, because the parts of the mechanism will be deformed. Moreover, the endurance of the stressed parts rapidly decrease. Therefore, the stiffness of the springs, as well as the geometry, of the MTU and STU were carefully optimized by iteration process in MSC ADAMS. The aim of this optimisation was to achieve as small forces in the mechanism as possible. Nevertheless, a minimal possible force should not have fallen below 1 N. It can be seen from the figures concerning the studied forces (i.e. Fig. A.2, Fig. A.3, Fig. A.4, Fig. A.6, Fig. A.7 and Fig. A.8) that the forces among the mechanism satisfied these requirements.

3.2.3 Investigation of Guided unit

It has been found from the simulation that the biggest force among the mechanism takes place in the contact between Slider and MEU. Hence the tension in this contact

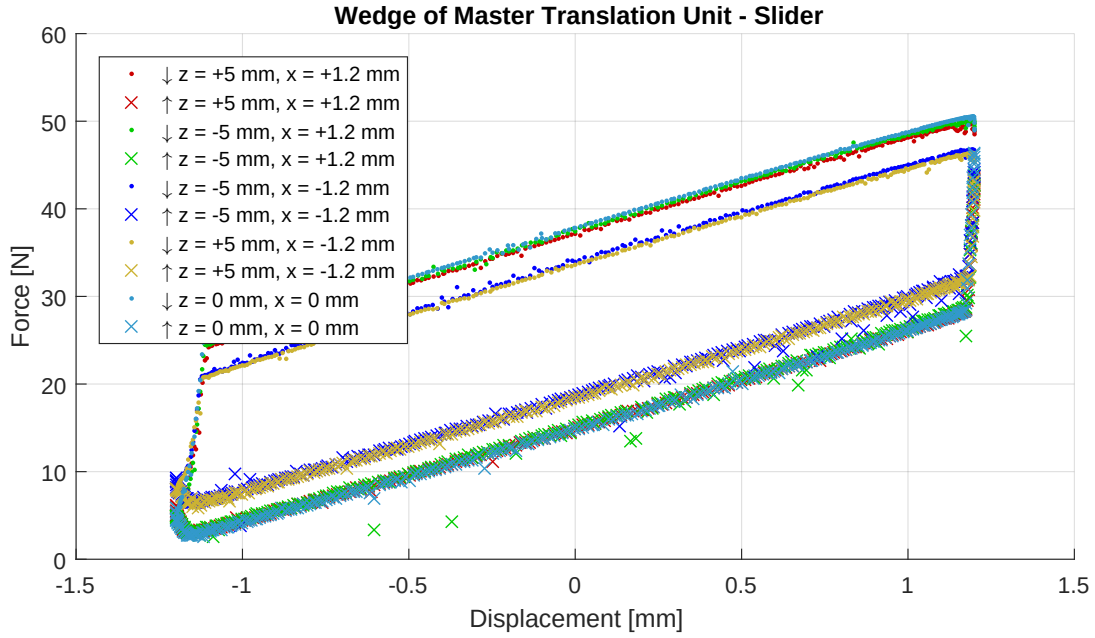

Fig. 3.6: Magnitude of force in the contact between the wedge of MTU and Slider in a varied positions and directions of movement among the mechanism. The ↑ and ↓ stands for increasing and decreasing displacement, respectively

was investigated. According to Hertzian Contact Theory [55], the maximal pressure in a contact between two balls is given by

$$p_0 = \left(\frac{6FE^{*2}}{\pi^3 R^2}\right)^{1/3}, \tag{3.2}$$

where F is total force exerted between the bodies and R is equivalent radius combining both radii of the bodies:

$$\frac{1}{R} = \frac{1}{R_1} + \frac{1}{R_2}. \tag{3.3}$$

E^* is a constant depending on the material constants of both bodies. Following expression is used.

$$\frac{1}{E^*} = \frac{1-\nu_1^2}{E_1} + \frac{1-\nu_2^2}{E_2}, \tag{3.4}$$

where ν_1, ν_2 and E_1, E_2 are Poisson's ratios and moduli of elasticity of the first and the second body, respectively.

The radius of the area of the contact is expressed as [55]

$$a = \left(\frac{3FR}{4E^*}\right)^{1/3} \tag{3.5}$$

The values of the normal stresses along the respective axes are [56]

$$\sigma_1 = \sigma_2 = \sigma_x = \sigma_y = -p_0 \left[\left(1 - \left| \frac{z}{a} \right| \tan^{-1} \frac{1}{|z/a|} \right) (1+\nu) - \frac{1}{2\left(1+\frac{z^2}{a^2}\right)} \right], \tag{3.6}$$

$$\sigma_3 = \sigma_z = \frac{-p_0}{1+\frac{z^2}{a^2}}, \tag{3.7}$$

where z stands for distance from the contact surface.

The maximal shear stresses are [56]

$$\tau_{\max} = \tau_{1/3} = \tau_{2/3} = \frac{\sigma_1 - \sigma_3}{2} = \frac{\sigma_2 - \sigma_3}{2} \tag{3.8}$$

Failure theory of Maximum shear stress (MSS) was used for the estimation whether a plastic deformation will occur or not. This theory assumes that the plastic deformation in a certain point of the ductile material takes place if

$$\tau_{max} \geq \frac{R_e}{2}. \tag{3.9}$$

This theory is not as exact as the theory of Distortion energy (DE) but it is much easier and more conservative [56].

Slider is a part of the sphere with a radius of $R_1 = 19,3\ mm$ that contacts the flat surface of the wedge. Thus the second radius (the flat surface of the wedge) is infinity $R_2 = \infty$. The Slider is made of brass EN CW614N with Poisson's ratio, module of elasticity and yield stress of approximately $\nu_1 = 0.342$, $E_1 = 106$ GPa and $R_e = 250$ MPa, respectively. The wedge is machined from steel C55 so that the material constants are as follows: $\nu_2 = 0,292$, $E_2 = 207$ GPa and $R_e = 450$ MPa.

The magnitude of force in boundary positions of the mechanism between the slider and master as well as slave wedge is depicted in Fig. 3.6 and Fig. A.5, respectively. Obviously, the force between the master wedge and slider (see 3.6) depends on a tendency of the movement of the slider because the vector of friction forces between the slider and other parts of mechanism depend on the tendency of movement as well. If ones push the master wedge, they have to overcome the friction forces. Ergo the maximal force on the slider and master wedge takes place when the mechanism is maximally pressed. This force has been evaluated by the simulation as $F_{max} = 50$ N (see Fig. 3.6). When the master wedge is eased, the force on it is stepped down by a magnitude of friction force and the only forces allowing the slider to move are the forces of compression springs. Therefore, the forces of compression springs have to be high enough in order to overcome the friction. Nevertheless, if the forces of the springs are increased, the friction is increased as well. This is the main reason why it is so important to reduce the friction in these parts of the mechanism

as good as possible. The simulation revealed that the static, as well as dynamic friction, have to be less than 0.2.

Since the maximal force is known, we can investigate stresses in the contact between the slider and master wedge. Fig. 3.7 shows the maximal stresses in the contact under the surface of the wedge (the red curves) and slider (the black curves), which are determined by the equations (3.6), (3.7) and (3.8). The horizontal lines in Fig. 3.7 show the condition (3.9), which is the boundary of plastic deformation. It is plain to see that steel wedge satisfy the condition and thus will not be plastically deformed. The brass slider does not satisfy the condition (see the black horizontal line in Fig. 3.7 that is under the maximal stress of τ_{max}), ergo the material under the contact will be plastically deformed. Therefore the brass sphere will be slightly crushed, which consequently increase the contact area. These consequences lead to a phenomenon called pitting which is a big problem in many devices such as bearings and train wheels [55]. Nevertheless, the slider in our application is static and thus any fracture is not likely to happen. The important conclusion from this analysis is that the flat surface of the steel wedge will not be crushed.

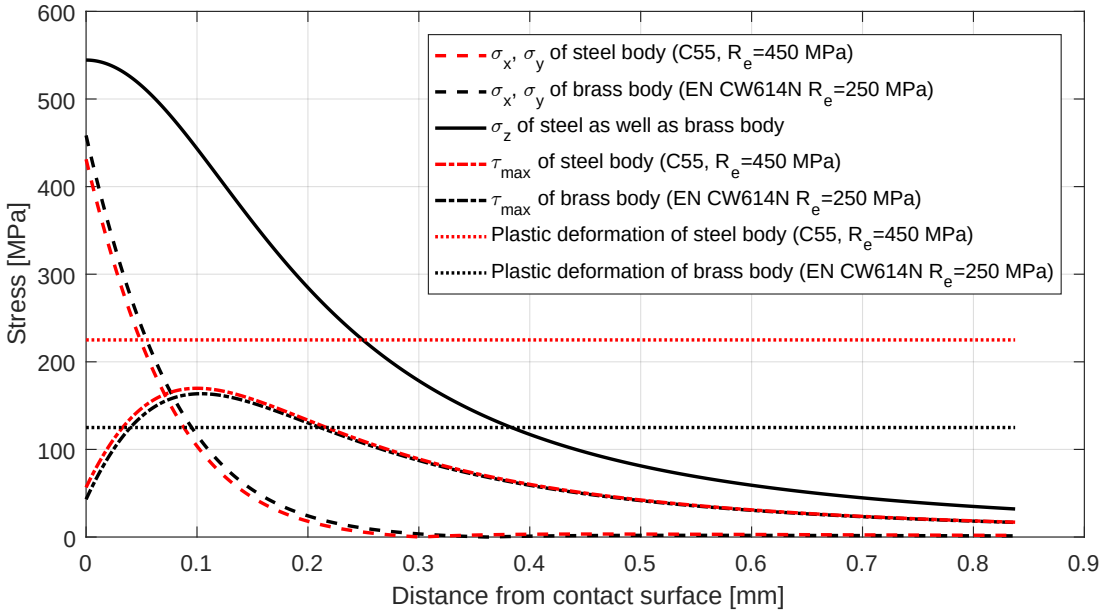

Fig. 3.7: Stresses in contact between slider and master wedge.

3.2.4 Friction

We discussed in previous chapters that the friction in the mechanism must be reduced as good as possible. The MSC simulation revealed that the static, as well as dynamic friction, should not be greater than 0.2. Therefore, we suggested brass-steel

contact in critical connections where the load is maximal, which ensures that the friction will be approximately 0.5 without lubrication [57]. That is why the slider is made of brass. However, a lubrication is still crucial. It has been proved that lubricated brass-steel can achieve the coefficient of friction smaller than 0,15 [58].

The important requirement for the lubricant, except of the reduction of friction, is the compatibility with the middle vacuum of approximately 0.1 mbar that occurs in the chamber during the purging process. The lubricant can evaporate or lose its properties in the vacuum. Therefore, it has to be protected by labyrinth seal or the vapour pressure of the lubricant has to be very low [57]. It would be very complicated to add the seal into the design of VUV module, so that a specialised grease for the vacuum has been chosen. For instance, Apiezon AP101 satisfy all requirements.

3.3 Control software and electronics

The block diagram of modules, devices and software of the VUV module as well as the experimental setup is depicted in the Fig. 3.8. The spectrometer of the VUV module is controlled by the Digital Image Sensor Board (DISB) Evaluation Kid provided by Ibsen. This package comprises a software as well as a hardware including:

- the interface board that is connected to the DISB by ribbon cable. This board also provides the connection to the power supply and other pins controlling the features i.e., external trigger, temperature read-out and writing as well as reading of other detector properties.
- DLN-4M SPI-USB adapter that provides the communication data transfer between the detector and the PC through the USB port. This adapter is connected to the interface board
- The DISB evaluation software that reads the data from the detector. This software can also do the wavelength calibration and save the data in the hard-drive of the PC.

The synchronization of the devices, i.e. the flash lamp and the Q-switch of the laser and the detector of the VUV module, was controlled by Digital Delay Generator (DDG). Values of proper delays were set in the Interaction chamber controller and written into the firmware of the DDG by the PC and the Control electronics.

Neither DISB nor interface board were compatible with the digital delay generator (DDG) because the two pins i.e. TRIGGER and GND, corresponding to the trigger and ground, respectively, of the interface board must be pulled down in order to initiate a measurement. The DDG gives, however, very short well-defined pulses of the voltage of 5 V. Therefore, the converter must have been developed. The block

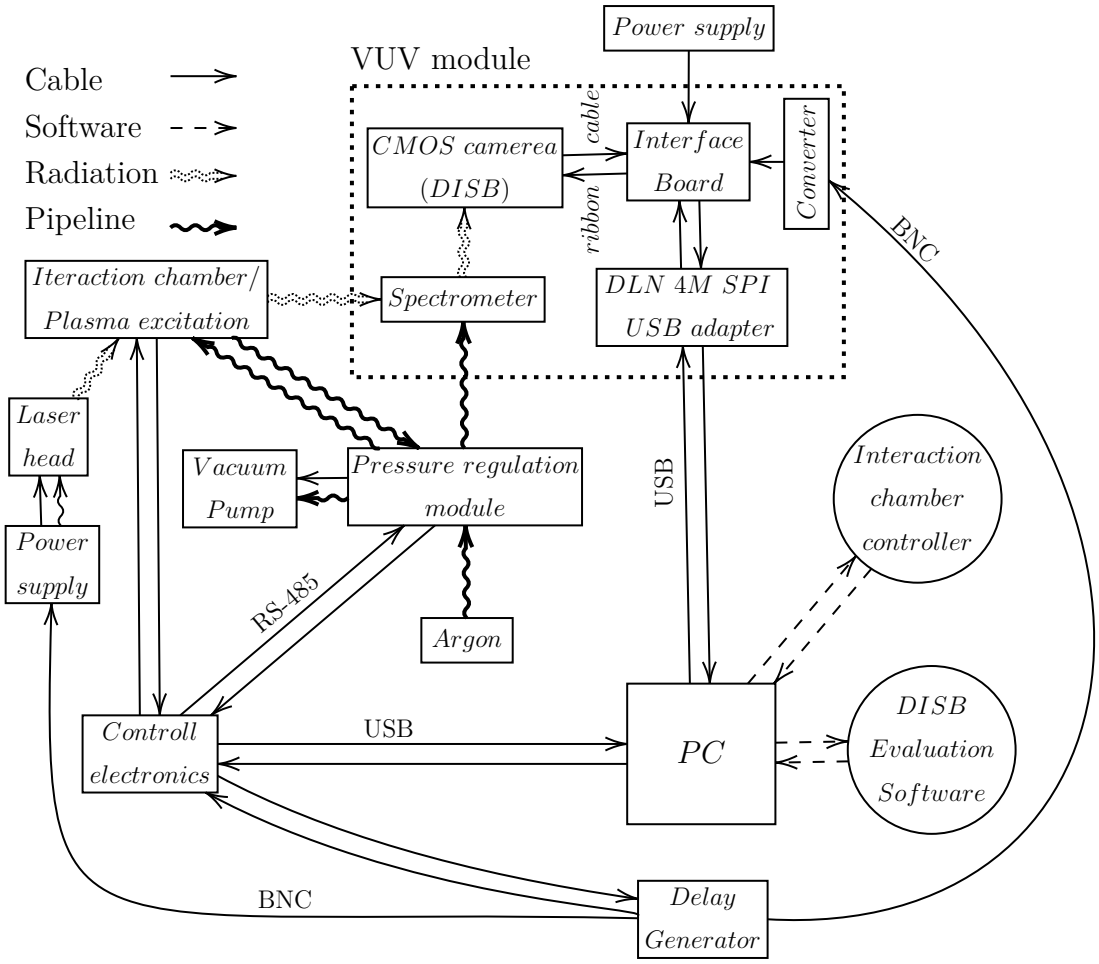

Fig. 3.8: Block diagram of the experimental setup in a configuration with the VUV module. The modules and devices are surrounded by a rectangular. The software is surrounded by a circle.

diagram of the converter is shown in the Fig. 3.9. The MOSFET transistor in this circuit shorts the TRIGGER and GND when the pulse voltage 5V from the DDG is applied on the transistor. This initiate a measurement.

The manipulator in the interaction chamber and the Pressure regulation module (MPR) were controlled by the control electronics that communicated with the Interaction chamber controller in the PC. The MPR automatically pumped the interaction chamber and then purged the chamber as well as the VUV module by argon.

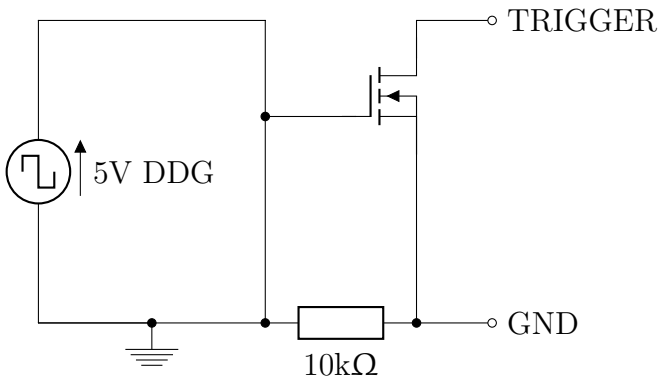

Fig. 3.9: Circuit diagram of the converter.

3.4 Manufacturing and implementation of the VUV module

The optomechanics of the experimental module was either manufactured in the workshop of Institute of Physical Engineering BUT or bought by Thorlabs company. The optomechanical parts of the final module have not been in the manufacturing possibilities of the workshop. Therefore, according to the technical drawings of these parts, they were ordered in the manufacturing company SolidCon s.r.o., which is specialized in the CNC machining. Other parts of the final module including the vendor as well as the price are summarised in Tab. 3.1.

Tab. 3.1: List of manufactured and purchased parts of the VUV module

Item	Vendor	price (€)
Manufactured		
Mechanical parts (optomechanics)	Solidcon, s.r.o.	2474
Sheet-metal parts	TopCNC s.r.o.	17
Purchased		
Spectrometer Freedom HR-DUV	Ibsen	4670
UV solar FA-2 objective	Solar	300
20 mm Calcium Fluoride Window	Edmund optics	110
Optomechanics	Thorlabs	29
Air fittings and pipelines	GMS	14
Springs	Vanel	48
O-rings	Alfa Agro Brno s.r.o.	5
Vacuum grease	Kurt J Lesker Company Ltd	49
	total:	7713 €

The experimental module was assembled and tested in December 2017. Then, the second iteration of the module was built in April 2018. Both of them were carried out and experimentally tested on devices in Laboratory of laser spectroscopy in Brno. The completed final module is shown in Fig. 6.1.

The overall price of the final module was 7664 €. The most expensive items are both the spectrometer (i.e. 4670 €) and the machined optomechanics (i.e. 2474 €)

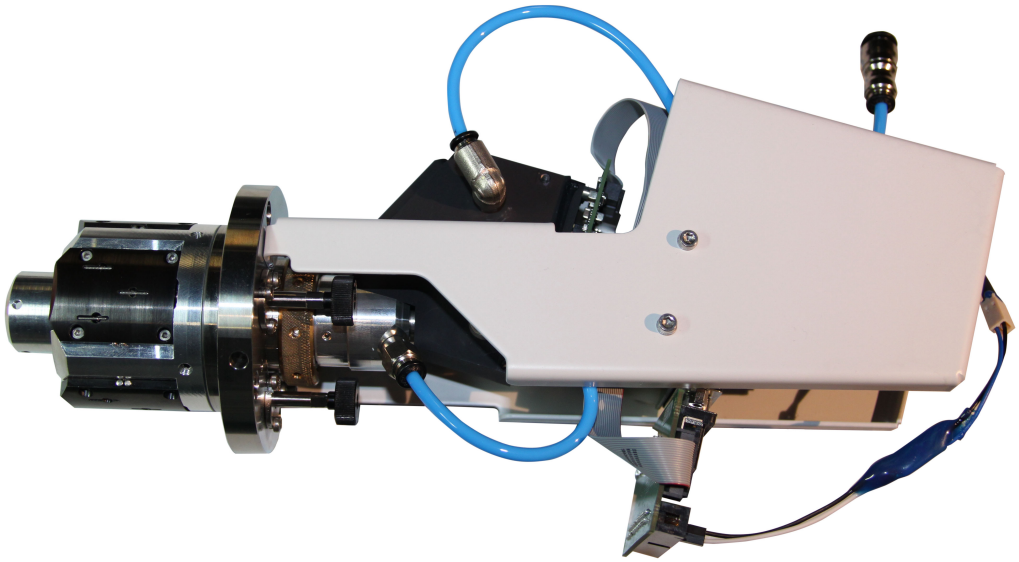

Fig. 3.10: The final module completed in the Laboratory of laser spectroscopy in Brno.

4 Experimental

4.1 Samples

The measured samples, from which the calibration curve was determined, comprised five certified low alloyed steels standards, provided by BAM(Federal Institute for Materials Research and Testing, DE) and by SPL-LABMAT s.r.o.(CZ). The list of these samples including the concentrations is in the Tab. 4.1.

Tab. 4.1: List of samples used for determination of calibration curve and their composition in wt.%

Sample	C	P	S	Si	Mn	Cr	Ni
PT-061	0.448	0.0125	0.0243	0.241	0.615	0.227	0.086
PT-231	0.183	0.0147	0.0083	0.335	1.066	0.216	0.034
PT-211	0.357	0.0191	0.009	1.255	1.213	0.076	0.0215
PT-221	0.322	0.0124	0.0039	0.182	0.839	1.169	0.028
BAM SUS-1 R	0.9	0.02	0.017	0.8	1.1	1.7	2.9

The LIBS spectrum of stainless steel and cast iron was also investigated. Certified stainless steel provided by BAM and the cast iron, which composition was determined by SD-OES, were used. The composition in wt.% is shown in Tab. 4.2

Tab. 4.2: List of stainless steel and cast iron samples used in analysis and their composition in wt.%

Sample	C	P	S	Si	Mn	Cr	Ni
BAM C1	0.092	-	-	0.46	0.74	12.35	12.55
Cast iron no.1	3.5	0.208	0.0723	2.25	0.459	0.214	-
Cast iron no.2	2.99	0.0428	0.0066	2.47	0.217	0.0324	-
Cast iron no.3	3.56	0.36	0.124	2.06	0.61	0.12	-
Cast iron no.4	2.84	0.0434	0.0152	5.34	0.255	0.346	-

The flat surfaces of all samples were polished and cleaned by isopropyl alcohol prior to the measurement in order to overcome any fluctuations of plasma due to the roughness.

4.2 Setup

Samples were measured by the device for comprehensive LIBS analysis in two configurations offering overall spectral range from 178 nm to 900 nm. The device is

schematically depicted in the Fig. 4.1. The main part is the interaction chamber (IC), which was described in the chapter 2.2. The radiation of the laser head (LH) (Solar LQ-529) powered by the laser power supply (PS) was introduced by dielectric mirrors of periscope (P) and focused on the surface of a sample (S) by focusing optics (FS) (24.5 mm; Sill Optics, Germany). Consequently, the luminous plasma was excited on the surface. In the Setup I offering the spectral range from 250 to 900 nm, the radiation was collected by a collection optics (CO) (100 mm CaF_2 and 75 mm UVFS; Thorlabs, USA) and introduced into the spectrometer (S) (190–1100 nm, 5000 $\lambda/\Delta\lambda$; Emu-65, Catalina Scientific, USA) via optical fibre. The spectrum was captured by EMCCD detector (200–1000 nm, max 30 Hz repetition rate; Falcon Blue, Raptor Photonics, Ireland). The VUV module (see chapter 3.2) offering the spectral range of 178-400 nm was used in the second configuration (Setup II).

Ambient air conditions were controlled by the Pressure Regulation Module (MPR). The synchronization of the LIBS experiment was performed by the control electronics (CE) developed in the Laboratory of laser spectroscopy in Brno. (CE) also controlled the Pressure Regulation Module (MPR) and 3-axes sample stage (SS) holding the sample (S).

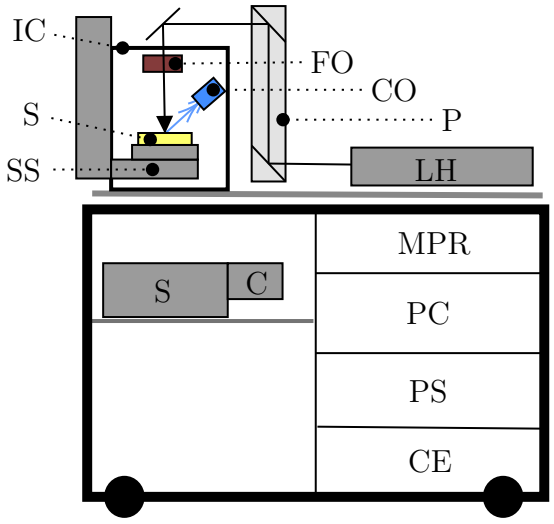

Fig. 4.1: Schematic diagram of experimental device, where: LH - laser head; S - spectrometer; C - camera/ detector; MPR - Pressure Regulation Module (gas purge); PC - computer; PS - laser power supply; CE - control electronics; P - periscope with reflective mirrors; SS - 3-axes sample stage; S - sample; IC - LIBS interaction chamber; FO - focusing optics, and CO - collection optics/ VUV module.

5 Results

5.1 Analysis in the UV-VIS-NIR spectral range

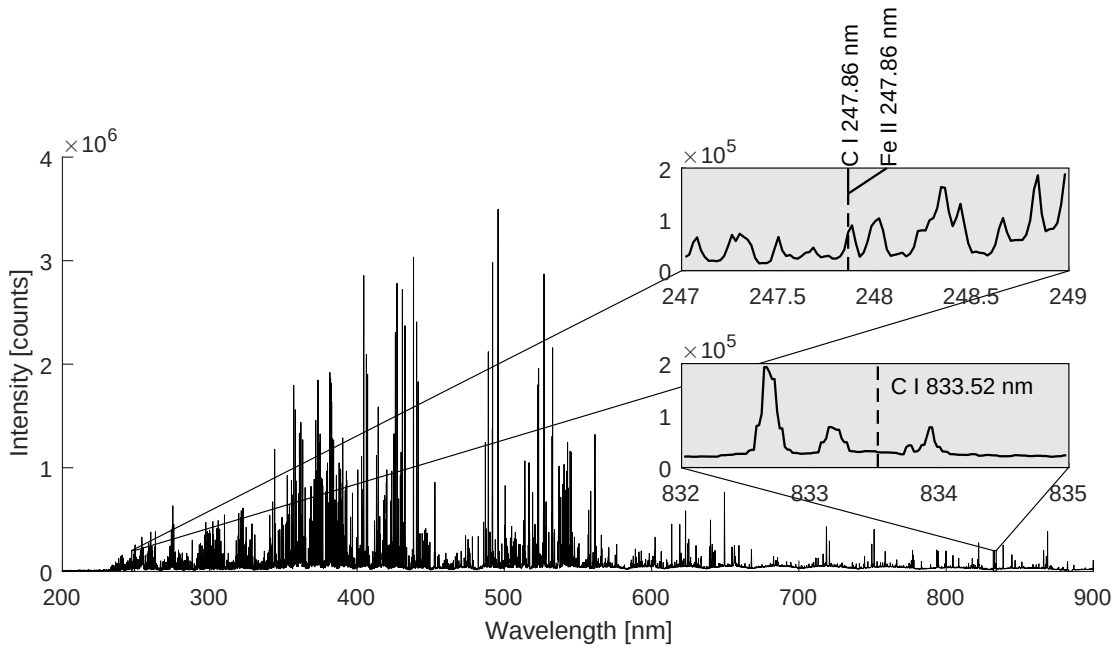

Fig. 5.1: LIBS spectrum of of Cast iron no.3 in UV-VIS-NIR spectral range

It has already been pointed out that the carbon content in ferrous alloys cannot be determined with LIBS by use of UV-VIS-NIR. We investigated this statement by the measurement of four cast iron with high concentration of C (see Tab. 4.2).

The spectrum of Cast iron no.3 measured by Setup I configuration is depicted in the Fig. 5.1. According to the NIST database, only eighteen emission lines of C I in the 200-900 nm range should be observable. The most prominent lines are at the wavelengths 247.9 nm and 833.5 nm. The upper portion of the spectrum in Fig. 5.1 shows a strong line at the position of 247.9 nm, which ought to be the C I 247.9 nm emission line. Nevertheless, the intensity of this line does not correlate with C concentration of the studied samples. It turned out that the intensity correlates with the iron concentration. Another prominent emission of carbon might have been observed at the 833.5 nm (see lower portion of the Fig. 5.1) One can see that the C I 833.5 emission line was not exited at all. We checked all the lines of C I in the range from 200 nm to 900 nm, but no emissions of C were observed. Therefore, either no carbon lines were exited, or they interfered with stronger iron lines and thus no useful information of the carbon concentration in iron matrix was visible.

The experiment was done in ambient atmosphere of helium with the pressure of 950 mbar, the energy of laser pulse was 20 mJ and gate delay was 2µs.

5.2 Analysis in the VUV spectral range

This research aims mainly at investigation of carbon, sulphur and phosphorus concentration in steel because those must be necessarily investigated in the VUV.

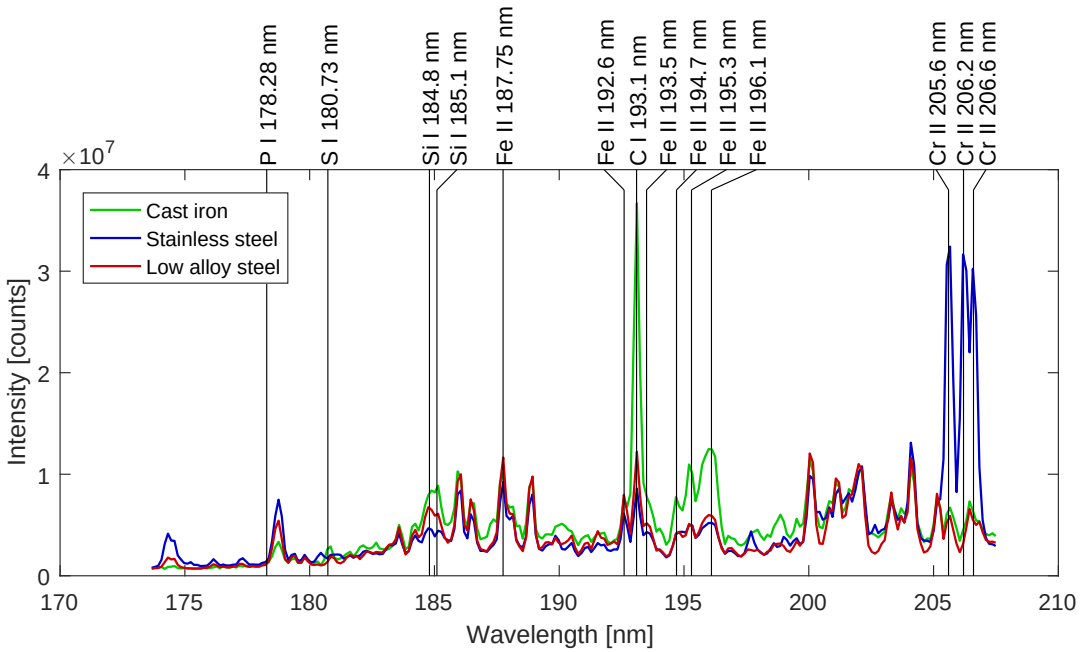

Fig. 5.2: spectrum in VUV of Cast iron no.3 (green), stainless steel C1 (blue), and low alloyed steel PT-61 (red).

Spectra of the cast iron no.3, the stainless steel BAM C1 and low alloy steel PT-061 were measured in order to distinguish the emission lines in VUV (see Fig. 5.2). Since the chemical composition of those ferrous alloys are quite distinct from each other, the emissions can be easily recognized. For instance, a cast iron has in general high concentration of C as well as Si so that the intensities of the corresponding lines (i.e. C I 193.1 nm, Si I 184.8 nm) are higher. On the other hand, a stainless steel comprises significant portion of Cr and thus the emission lines of Cr (e.q. Cr II 205.6 nm) are very intense. The Fig. 5.2 also shows the position of P I 178.28 nm and S I 180.73 nm, which, however, are not visible. Most likely, they were not be excited due to inappropriate experimental conditions (i.e. gate delay, pulse energy) for these emissions or because the LODs for S and P were not low enough. The list of appropriate emissions for further analysis are in Tab. 1.1.

The most prominent line of C is at the wavelength of 193.1 nm. We found that the intensity of this line does not correlate with the concentration of the C content in top layers of the sample. Fig. 5.3 shows that the intensity is not invariable over the layers although the surface of the sample was carefully polished and cleaned prior to the measurement. The intensity reaches its maximum in a few first pulses

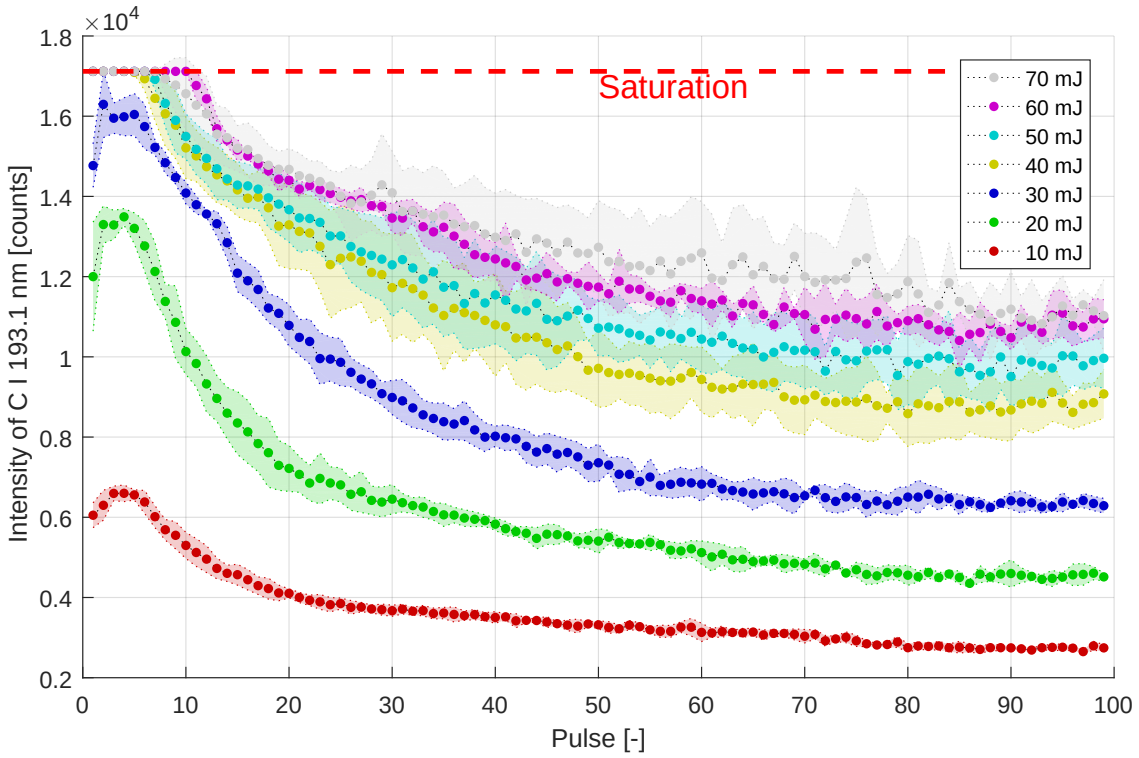

Fig. 5.3: The intensity of C I 193.1 nm emission line depending on the laser pulse order. The shaded areas show the error of the measurements.

and then rapidly decrease. The falling of the intensity gradually slow down and the value of intensities slowly approaches an asymptote. It has been quite surprising that similar evolution was not observed for other emission lines in a spectrum.

We observed that the correlation between the intensity of C I 193.1 nm and the concentration of C is better when the measured intensities are closer to the asymptote. The correlation is shown in Fig. 5.4. The calibration curve in the left portion of this figure is made up of first ten measurements (first ten pulses, i.e. upper layers of the sample). One can see that there is a poor correlation. The second calibration curve in the middle of the Fig. 5.4 discards the first 30 measurements and thus the correlation rapidly increases. The last calibration curve in the right portion of the Fig. 5.4 that achieved the best correlation, takes in account only the last ten measurements. Therefore, it turns out that the better results can be achieved by the higher number of initiate pulses before measurement. In fact, this approach of hight number of initiate pulses was applied in papers devoted to steel analysis [5]. However, the phenomenon concerning behaviour of the C I 193.1 nm emission line was not explained, as far as we know.

The LOD was computed from the curves of growth in Fig. 5.4 according to the theory examined in chapter 1.4. All values are written in the respective graph of

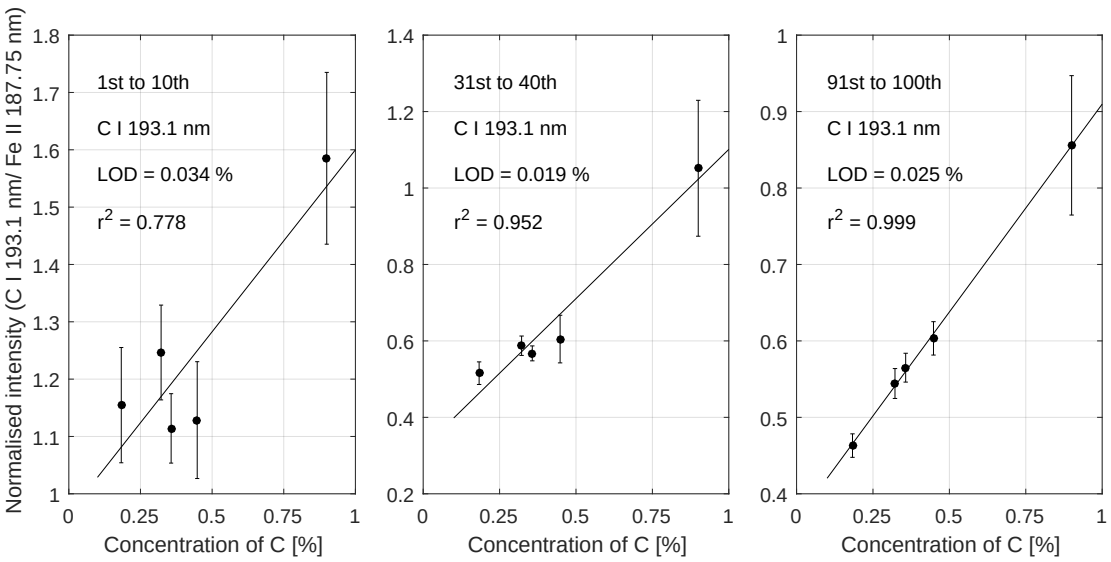

Fig. 5.4: Curve of growth of the sample

the calibration curve. The samples were measured by two maps, placed each in a different portion of the sample, that comprise each 5×5 points. Every point was measured one hundred times so that the dataset comprised 2500 spectra for each sample. For every measurement in this section, the gate delay was 3.2 μs and the gate time was 50 μs. The energy of the laser was reduced by optical attenuator down to the value of 50 mJ. All samples were measured in ambient atmosphere comprised pure argon with the pressure of 950 mbar. Prior to the calibration curve determination, the dataset was normalised to the intensity of the emission line of Fe II 187.75 mm.

5.2.1 Spectral outliers filtering using PCA

Principal component analysis (PCA) approach was used for spectral outlier filtering in order to reduce errors of the measurements in the calibration curves. The principles of PCA were discussed in chapter 1.4.3.

The data were prepared the same way as in the previous investigation. I.e. last ten measurements of individual points among the 5×5 map were separated and normalised to the intensity of the Fe II 187.75 mm emission line. The range of wavelengths of every measurement was reduced to the range of 185-210 nm and then, the PCA using SVD (Singular-value decomposition) algorithm performed by Matlab was computed.

The first three components of Loadings and Scores representing over 99 % of the overall information, are depicted in Fig. 5.5 and Fig. 5.6, respectively. The first component is strongly associated with iron emissions (see upper portion of Fig. 5.5).

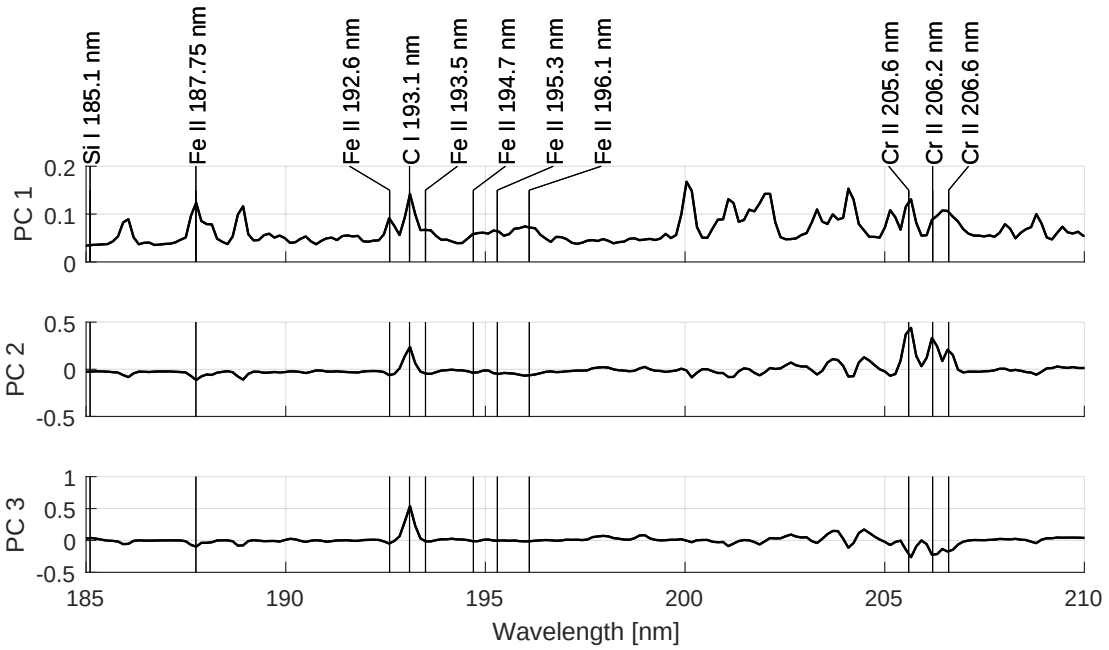

Fig. 5.5: PCA Loadings of the normalised dataset comprised by five steel samples and labelled emission lines that are responsible for the extraordinary positions of the clusters in the Scores plot

Therefore, values of PC 1 for every cluster are similar since the concentration of Fe in every steel sample is similar as well. The second and the third component do not contain as intense Fe emissions as the first component (see lower portion of Fig. 5.5). They are rather associated with the concentration of carbon and chromium. Hence the second and third component already distinguish the clusters according to the individual samples (see Fig. 5.6), since the concentration of C as well as Cr significantly varies over the samples.

Another important information given by Scores is the spread of the individual measurements. One can see in Fig. 5.6 that the points of BAM SUS-1 R sample are more scattered than the measurements of other samples. We found the same observation by the standard deviations in the curves of growth in Fig. 5.4. Moreover, the measurement of the BAM SUS-1 R produced obvious outlier represented by the isolated point in the Scores plot.

The coordinates of the center of each cluster was found by the median computed from values of the three components corresponding to the respective cluster. Then, the 40 points nearest to the center (16% of the original dataset) were isolated and other measurements for every cluster were discarded from the dataset. The new filtered dataset was processed from which the curve of growth was evaluated. The new curve of growth is depicted in Fig. 5.7. One can see that the standard deviation

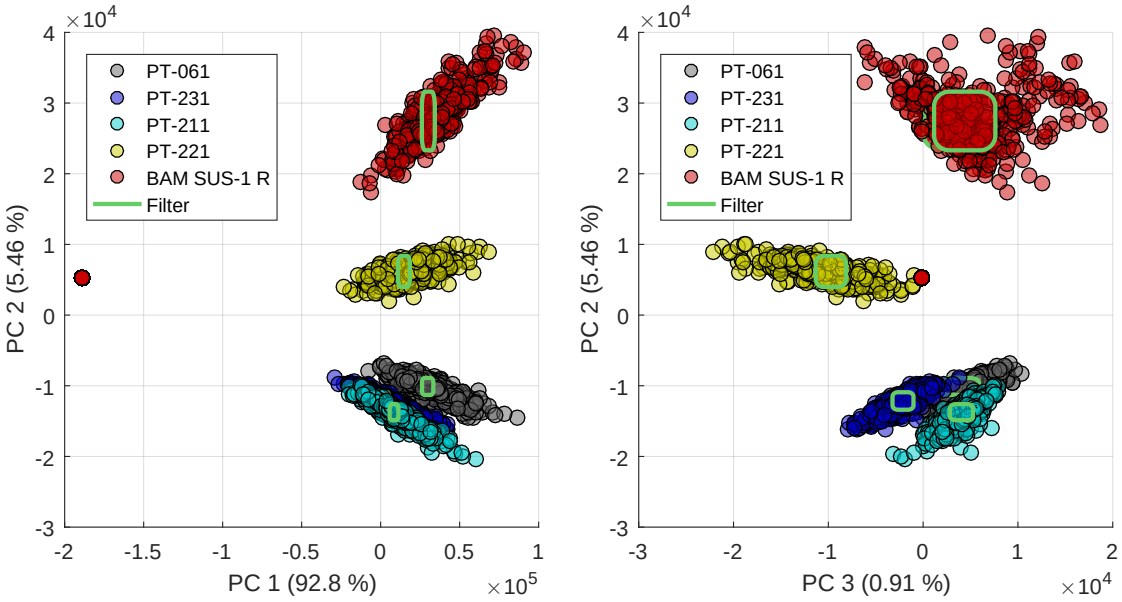

Fig. 5.6: PCA Scores of the normalised dataset comprised by five steel samples

of every sample was reduced, though the coefficient of determination is not as good as in the curve of growth prior to the filtering.

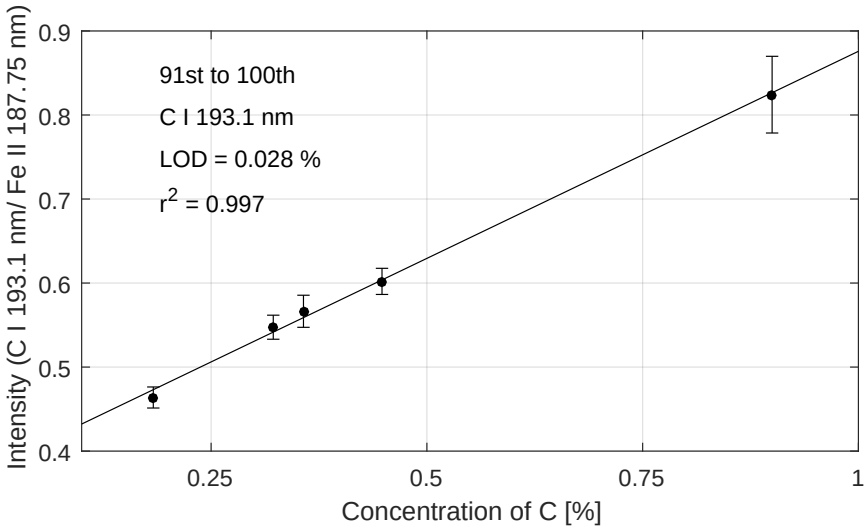

Fig. 5.7: Curve of growth of the filtered dataset

6 Discussion

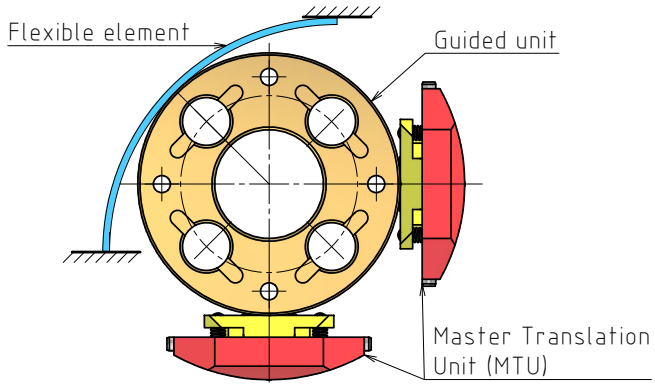

Fig. 6.1: Proposed concept for the next iteration that replaces the STU by the flexible element.

The mechanics of VUV module was completed without significant trouble and all requirements concerning the accuracy, vacuum compatibility, etc., were satisfied. However, several complications, as well as hints for the improvement, arose during the assembling. Those are summarized as follows.

- The adjustment shaft got stuck when a housing, that guides and seals the shaft, was tightened. It occurred, because the geometrical tolerances of the flange (i.e., parallelism, perpendicularity, and flatness) were not as precise as expected and thus the clearance between the shaft and the housing (H7/g6) was not big enough. This issue was solved by a hole drilled in the housing, that provided with the higher clearance (more than 0.1 mm)
- A mounting jig would facilitate the assembling. This jig would hold the shaft of the guided unit during the installation and also enable to adjust the amount of the springs (S5) compression.
- The movement in Z direction controlled by union nut was quite tough, meaning one needed to make a lot of force in order to turn the union nut. Most likely, it is caused by the key scraping against the keyseat that is milled across the thread in the shaft. It might be solved by another shape of either the key or the keyseat.
- Master translation units (MTU) worked smoothly but the functioning of Slave translation units (STU) was not as smooth as expected and hence a stronger compression springs must have been used. It shall be appropriate in next iteration to consider another concept of STU. For instance, they could be replaced by a flexible element such as sheet metal pressing against the Guided unit (GU). This concept is shown in Fig. 6.1. The deformation variation

of such a flexible element shall be relatively small and thus the forces will be approximately the same in any position of the mechanism. This might make the functioning of the entire mechanism smoother. Furthermore, the mechanism might be more precise in this case because deformations of the parts would be negligible if the forces were rather small.

The issue concerning the higher intensities of the C I 193.1 nm emission line from the plasma on the top layers of the sample was not satisfactorily explained. This behavior is depicted in Fig 5.3. Obviously, either the top layers contained higher concentrations of C or the properties of the plasma were changing during the measurement. Possibly, if the plasma was excited in the crater deepened by the laser pulses, the plasma would change its properties due to this cavity and thus the proportion of the intensities between the emission lines among the spectrum would change. However, this theory does not explain the questions: Why is not there any correlation between the intensities and the concentration at the beginning of this measurement, and why does that behavior occur only for the C I 193.1 nm emission line? These questions shall be a topic of further investigation in the future.

7 Conclusion

This diploma thesis' aim was an investigation of light elements in ferrous alloys using Laser-Induced Breakdown Spectroscopy (LIBS). The particular task was concerned with the development and implementation of a new module into the device serving for LIBS analyse in the Laboratory of laser spectroscopy in Brno. The module would enable a spectral analysis of the wavelengths below 200 nm which is necessary for both the steel analysis and many more applications of LIBS.

The first part of this thesis deals with the theoretical background in which the basics of optical emission spectroscopy (OES) and some traditional techniques of steel analysis were outlined. This part also aimed to investigate and sort the theory about the absorption of vacuum ultraviolet (VUV) radiation by the air and optical glasses, which was essential for the development of the module.

An introduction of the proposed concepts was described in the second part. Subsequently, an experimental module was designed, assembled and tested in the interaction chamber in order to put the concept to the test and to reveal some hidden challenges concerning the analysis in the VUV.

According to the results that arose from the testing of the experimental module, the second iteration of the module was proposed in the third part. This final module was based on the unique wedge mechanism enabling the collection lens to be precisely adjusted in three axes. The lens is placed inside the chamber and collects the plasma radiation. Finally, the module was made up in cooperation with an external manufacturer.

The last part of this thesis concerned experimental measurements of five steel samples in order to demonstrate the performances of the final module. The measured spectra were processed and interpreted by the standard calibration curves and the chemometrics including the principal component analysis (PCA) approach. The limit of detection (LOD) for carbon was estimated as 0.028 wt%, which is worse in comparison with other research works concerned with the carbon determination in steel (i.e. better than 10 μg/g [6]). However, there is plenty of room for improvement because a comprehensive optimization of the experimental conditions has not been carried out so far.

All goals were satisfied in this thesis although several questions remained unanswered. Particularly, we could not explain the behavior of the carbon emission during the analysis. The comprehensive study is going to be necessary to figure this issue out. Both this issue and the optimization of the experimental conditions for steel analyse shall be the incentives for a future work.

Bibliography

[1] *ASM Handbook, Volume 9: Metallography and Microstructures*. Vol. 2. 2001, p. 3470. ISBN: 0871700077. DOI: 10.1016/S0026-0576(03)90166-8.

[2] Bernard Jurgen Schulz. "Alloy effects in temper embrittlement". PhD thesis. University of Pennsylvania, 1972, p. 193.

[3] Andrzej W. Miziolek et al. *Laser-Induced Breakdown Spectroscopy (LIBS)*. 1. 2006, p. 620. ISBN: 9780874216561. DOI: 10.1007/s13398-014-0173-7.2.

[4] David A. Cremers and Leon Radziemski. *Handbook of Laser-Induced Breakdown Spectroscopy*. 2013, p. 325. ISBN: 9781119971122.

[5] Reinhard Noll. *Laser Induced Brekdown Spectroscopy*. 2012, p. 556. ISBN: 9783642206672. DOI: 10.1007/978-3-642-20668-9Springer.

[6] Volker Sturm, Laszlo Peter, and Reinhard Noll. "Steel analysis with laser-induced breakdown spectrometry in the vacuum ultraviolet". In: *Applied Spectroscopy* 54.9 (Sept. 2000), pp. 1275–1278. ISSN: 00037028. DOI: 10.1364/AO.42.006199.

[7] M. Hemmerlin et al. "Application of vacuum ultraviolet laser-induced breakdown spectrometry for steel analysis - Comparison with spark-optical emission spectrometry figures of merit". In: *Spectrochimica Acta - Part B Atomic Spectroscopy* 56.6 (2001), pp. 661–669. ISSN: 05848547. DOI: 10.1016/S0584-8547(01)00217-8.

[8] Reinhard Noll et al. "Laser-induced breakdown spectrometry — applications for production control and quality assurance in the steel industry". In: *Spectrochimica Acta Part B: Atomic Spectroscopy* 56.6 (2001), pp. 637–649. ISSN: 05848547. DOI: 10.1016/S0584-8547(01)00214-2.

[9] Mohamed A. Khater. "Laser-induced breakdown spectroscopy for light elements detection in steel: State of the art". In: *Spectrochimica Acta - Part B Atomic Spectroscopy* 81 (2013), pp. 1–10. ISSN: 05848547. DOI: 10.1016/j.sab.2012.12.010.

[10] X. Jiang et al. "Double-pulse laser induced breakdown spectroscopy with ambient gas in the vacuum ultraviolet: Optimization of parameters for detection of carbon and sulfur in steel". In: *Spectrochimica Acta - Part B Atomic Spectroscopy* 101 (2014), pp. 106–113. ISSN: 05848547. DOI: 10.1016/j.sab.2014.07.002.

[11] Saara Kaski, Heikki Hakkanen, and Jouko Korppi-Tommola. “Determination of Cl/C and Br/C ratios in pure organic solids using laser-induced plasma spectroscopy in near vacuum ultraviolet”. In: *Journal of Analytical Atomic Spectrometry* 19.4 (2004). ISSN: 0267-9477. DOI: 10.1039/b315410f.

[12] Juraj Jasik et al. “Vacuum ultraviolet laser-induced breakdown spectroscopy analysis of polymers”. In: *Spectrochimica Acta - Part B Atomic Spectroscopy* 64.10 (2009), pp. 1128–1134. ISSN: 05848547. DOI: 10.1016/j.sab.2009.07.013.

[13] Leon Radziemski et al. “Use of the vacuum ultraviolet spectral region for laser-induced breakdown spectroscopy-based Martian geology and exploration”. In: *Spectrochimica Acta - Part B Atomic Spectroscopy* 60.2 (2005), pp. 237–248. ISSN: 05848547. DOI: 10.1016/j.sab.2004.12.007.

[14] Thomas R. Dulski. “Steel and Related Materials”. In: *Analytical Chemistry* 63.12 (1991), pp. 65–86. ISSN: 15206882. DOI: 10.1021/ac00012a005.

[15] M. Hemmerlin, L. Paulard, and G. Schotter. “Determination of ultra-low carbon and nitrogen contents in steel: combustion versus electrical spark source optical emission spectrometry for steelmaking process control”. In: *J. Anal. At. Spectrom.* 18 (2003), pp. 282–286. DOI: 10.1039/B210809G.

[16] Christopher; Erwin Loewen Palmer. “Diffraction Gratings for OEM and Scientific Applications”. In: *Catalog* 031101 (1947), p. 31101.

[17] John James. *Spectrograph Design Fundamentals*. Cambridge: Cambridge University Press, 2007, p. 191. ISBN: 9780511534799. DOI: https://doi.org/10.1017/CBO9780511534799.

[18] J. M. Lerner. “The Optics of Spectroscopy: A Tutorial V2.0”. In: (1988), p. 55.

[19] George R. Harrison. “The Production of Diffraction Gratings: II The Design of Echelle Gratings and Spectrographs”. In: *Journal of the Optical Society of America* (1949). ISSN: 0030-3941. DOI: 10.1364/JOSA.39.000522.

[20] Stuart Barnes. “The design and performance of high resolution échelle spectrographs in astronomy”. In: (2004), p. 265. URL: http://ir.canterbury.ac.nz/handle/10092/5576.

[21] John M Harlander et al. “SHIMMER : a spatial heterodyne spectrometer for remote sensing of Earth ’ s middle atmosphere”. In: 41.7 (2002).

[22] John M Harlander et al. “First results from an all-reflection spatial heterodyne spectrometer with broad spectral coverage.” In: *Optics express* 18.6 (2010), pp. 6205–6210. ISSN: 10944087. DOI: 10.1364/OE.18.006205.

[23] Patrick D. Barnett, Nirmal Lamsal, and S. Michael Angel. "Standoff Laser-Induced Breakdown Spectroscopy (LIBS) Using a Miniature Wide Field of View Spatial Heterodyne Spectrometer with Sub-Microsteradian Collection Optics". In: *Applied Spectroscopy* 71.4 (2017), pp. 583–590. ISSN: 19433530. DOI: 10.1177/0003702816687569.

[24] S.O. Kasap. *Optoelectonics and Photonics: Principles and Pratices*. 2013, p. 551. ISBN: 9780132151498.

[25] Richard L. Mccerry. *Raman spectroscopy in chemical bioanalysis*. Vol. 8. 5. 2000, pp. 534–539. ISBN: 0-471-25287-5. DOI: 10.1002/0471721646.

[26] Simon M Nelms. *Inductively Coupled Plasma Mass Spectrometry Handbook*. 2005. ISBN: 9781444305463. DOI: 10.1002/9781444305463. URL: http://doi.wiley.com/10.1002/9781444305463.

[27] D. A. Skoog, F. J. Holler, and S. R. Crouch. *Principles of Instrumental Analysis Sixth Edition*. 1998, p. 529. ISBN: 0030020786. DOI: 10.1016/S0003-2670(00)84936-3.

[28] Orazio Svelto. *Principles of lasers*. 2010, pp. 1–620. ISBN: 9781441913012. DOI: 10.1007/978-1-4419-1302-9.

[29] J Hermann et al. "Influence of irradiation conditions on plasma evolution in laser-surface interaction". In: *Journal of Applied Physics* 74.5 (1993), pp. 3071–3079. DOI: 10.1063/1.354594.

[30] Florian Trichard et al. "Evaluation of compact VUV spectrometer for elemental imaging by laser-induced breakdown spectroscopy: application to mine core characterization". In: *J. Anal. At. Spectrom.* (2017). ISSN: 0267-9477. DOI: 10.1039/C7JA00185A.

[31] P Dasgupta. "On use of Pseudo-Voigt Profiles in Diffraction Line Broadening Analysis". In: *Fizika A (Zagreb)* 9.2 (2000), pp. 61–666. ISSN: 1330-0008. DOI: 10.1177/097152150401100101.

[32] Frank C De Lucia, Jennifer L. Gottfried, and Andrzej W. Miziolek. "Analysis of Carbon and Sulfur in Steel Samples Using Bench Top Laser-Induced Breakdown Spectroscopy (LIBS)". In: *Materials Research* October (2009), p. 12.

[33] X K Shen et al. "Detection of trace phosphorus in steel using laser-induced breakdown spectroscopy combined with laser-induced fluorescence". In: *Appl. Opt.* 48.13 (2009), pp. 2551–2558. DOI: 10.1364/AO.48.002551.

[34] Jiaming Li et al. “Determination of Carbon Content in Steels Using Laser-Induced Breakdown Spectroscopy Assisted with Laser-Induced Radical Fluorescence”. In: *Analytical Chemistry* 89.15 (2017), pp. 8134–8139. ISSN: 15206882. DOI: 10.1021/acs.analchem.7b01932.

[35] Stanislaw Piorek. “Rapid sorting of aluminum alloys with handheld LIBS analyzer”. In: ().

[36] T.B. Lucatorto, J.T. Roberts, and T. J. McLlrath. “Capillary array - A new type of window for the vacuum ultraviolet”. In: *Applied Optics* 18.14 (1979), pp. 2505–2509. DOI: 10.1364/AO.18.002505.

[37] M a Khater et al. “Time-integrated laser-induced plasma spectroscopy in the vacuum ultraviolet for the quantitative elemental characterization of steel alloys”. In: *Journal of Physics D: Applied Physics* 33.18 (2000), pp. 2252–2262. ISSN: 0022-3727. DOI: 10.1088/0022-3727/33/18/308.

[38] Laszlo Peter, Volker Sturm, and Reinhard Noll. “Liquid steel analysis with laser-induced breakdown spectrometry in the vacuum ultraviolet”. In: *Applied Optics* 42.30 (Oct. 2003), p. 6199. ISSN: 0003-6935. DOI: 10.1364/AO.42.006199.

[39] H. Keller-Rudek et al. “The MPI-Mainz UV/VIS Spectral Atlas of Gaseous Molecules of Atmospheric Interest”. English. In: *Earth System Science Data* 5.2 (Dec. 2013), pp. 365–373. ISSN: 1866-3516. DOI: 10.5194/essd-5-365-2013.

[40] W. H. Parkinson K. Yoshino D. E. Freeman J. R. Esmond. “High resolution absorption cross section measurements and band oscillator strengths of the Schumann-Runge bands of O2”. In: *Planetary and Space Science* 31.3 (1983), pp. 339–353. ISSN: 00320633. DOI: 10.1016/0032-0633(83)90085-5.

[41] David G. Andrews. *An Introduction to Atmospheric Physics*. Vol. 53. 9. 2013, pp. 1689–1699. ISBN: 9788578110796. DOI: 10.1017/CBO9781107415324.004.

[42] Herbert Gross et al. *vol 1 Fundamentals of technical optics*. Vol. 2. 2006, pp. 1–690. ISBN: 9783527403783. DOI: 10.1002/3527606688.

[43] Joseph W Goodman. “Introduction to Fourier Optics McGraw-Hill Series in Electrical and Computer Engineering”. In: *Quantum and Semiclassical Optics Journal of the European Optical Society Part B* 8.5 (1996), p. 491. ISSN: 13555111. DOI: 10.1088/1355-5111/8/5/014.

[44] David W. Hahn and Nicoló Omenetto. “Laser-induced breakdown spectroscopy (LIBS), part II: Review of instrumental and methodological approaches to material analysis and applications to different fields”. In: *Applied Spectroscopy* 66.4 (2012), pp. 347–419. ISSN: 00037028. DOI: 10.1366/11-06574.

[45] Gary L. Long and J.D. Winefordner. “Limit of Detection A Closer Look at the IUPAC Definition”. In: *Analytical Chemistry* 55.7 (1983), 712 A - 724 A. ISSN: 0003-2700. DOI: 10.1021/ac00258a724.

[46] Sari Romppanen, Heikki Häkkänen, and Saara Kaski. “Singular value decomposition approach to the yttrium occurrence in mineral maps of rare earth element ores using laser-induced breakdown spectroscopy”. In: *Spectrochimica Acta Part B: Atomic Spectroscopy* 134 (2017), pp. 69–74. ISSN: 05848547. DOI: 10.1016/j.sab.2017.06.002.

[47] Jakub Klus et al. “Multivariate approach to the chemical mapping of uranium in sandstone-hosted uranium ores analyzed using double pulse Laser-Induced Breakdown Spectroscopy”. In: *Spectrochimica Acta - Part B Atomic Spectroscopy* 123 (2016), pp. 143–149. ISSN: 05848547. DOI: 10.1016/j.sab.2016.08.014.

[48] Pavel Pořízka et al. “Laser-Induced Breakdown Spectroscopy coupled with chemometrics for the analysis of steel: The issue of spectral outliers filtering”. In: *Spectrochimica Acta - Part B Atomic Spectroscopy* 123 (2016), pp. 114–120. ISSN: 05848547. DOI: 10.1016/j.sab.2016.08.008.

[49] Richard G. Brereton. *Applied Chemometrics for Scientists*. 2007, pp. 1–379. ISBN: 0470016868. DOI: 10.1002/9780470057780.

[50] Kevin Dunn. “Process Improvement Using Data”. In: July (2014), p. 381.

[51] Hervé Abdi and Lynne Williams. “Principal component analysis”. In: *Wiley Interdiscip Rev Comput Statistics* 2.4 (2010), pp. 433–459. ISSN: 1939-0068. DOI: 10.1002/wics.101.

[52] Z. HRABAL. *Úprava náhledového modulu sestavy LIBS*. [Bachelor thesis] Brno: BUT, FME, 2016. p.42.

[53] Volkmar Brucker. “To the use of Sellmeier formula”. In: *Springer* d (2011), pp. 0–7.

[54] Masahiko Daimon and Akira Masumura. “High-accuracy measurements of the refractive index and its temperature coefficient of calcium fluoride in a wide wavelength range from 138 to 2326 nm.” In: *Applied optics* (2002). ISSN: 0003-6935. DOI: dx.doi.org/10.1364/AO.41.005275.

[55] Valentin L. Popov. *Contact mechanics and friction : physical principles and applications*. 2010, p. 362. ISBN: 978-3-642-10802-0.

[56] J E Shigley, C R Mischke, and R G Budynas. *Shigle's Mechanical Engineering Design - 9th Ed.* Vol. New York, 2002, pp. 408–409. ISBN: 9780070568990. DOI: 10.1007/s13398-014-0173-7.2. arXiv: 9809069v1 [gr-qc].

[57] Michael J Neale. *The Tribology Handbook*. Second edi. 1995, p. 582. ISBN: 0-7506-1198-7.

[58] S. Senhadji, Farid Belarifi, and F. Robbe-Valloire. "Experimental investigation of friction coefficient and wear rate of brass and bronze under lubrication conditions". In: *Tribology in Industry* 38.1 (2016), pp. 102–107. ISSN: 03548996.

List of symbols, physical constants and abbreviations

c	speed of light
λ	wavelength
m	diffraction order
n	refractive index
N	number of illuminated grooves
R	Avogadro constant
R_{e}	yield stress
s	intersection length of a paraxial ray in the object space
s'	intersection length of a paraxial ray in the image space
E	module of elasticity
F	force
f	focal length
$f_{\#}$	f/number
h	Planck constant
I	irradiation
w	waist of the Gaussian beam
σ	normal stress
$\sigma(\lambda)$	absorption cross-section
τ	shear stress
ν	Poisson ratio
AAS	Atomic Absorption Spectroscopy
AES	Atomic Emission Spectroscopy
BUT	Brno University of Technology
DDG	Digital Delay Generator
DISB	Digital Image Sensor Board
FWHM	Full Width At Half Maximum
GU	Guided Unit
HU	Horizontal Unit
LA-ICP-MS	Laser Ablation Inductively Coupled Plasma Mass Spectrometry
LIBS	Laser-Induced Breakdown Spectroscopy
LOD	Limit of Detection
MTU	Master Translation Unit
OAS	Optical Absorption Spectroscopy
OES	Optical Emission Spectroscopy
PCA	Principal Component Analysis

PMT Photomultiplier Tube
SD-OES Spark-Discharge Optical Emission Spectroscopy
SHS Spatial Heterodyne Spectrometer
STU Slave Translation Unit
SVD Singular-Value Decomposition
UV-VIS-NIR Ultraviolet-Visible-Near Infrared radiation
VUV Vacuum Ultraviolet radiation
XRF X-ray fluorescence spectroscopy

List of appendices

A Results of dynamic simulation from MSC ADAMS

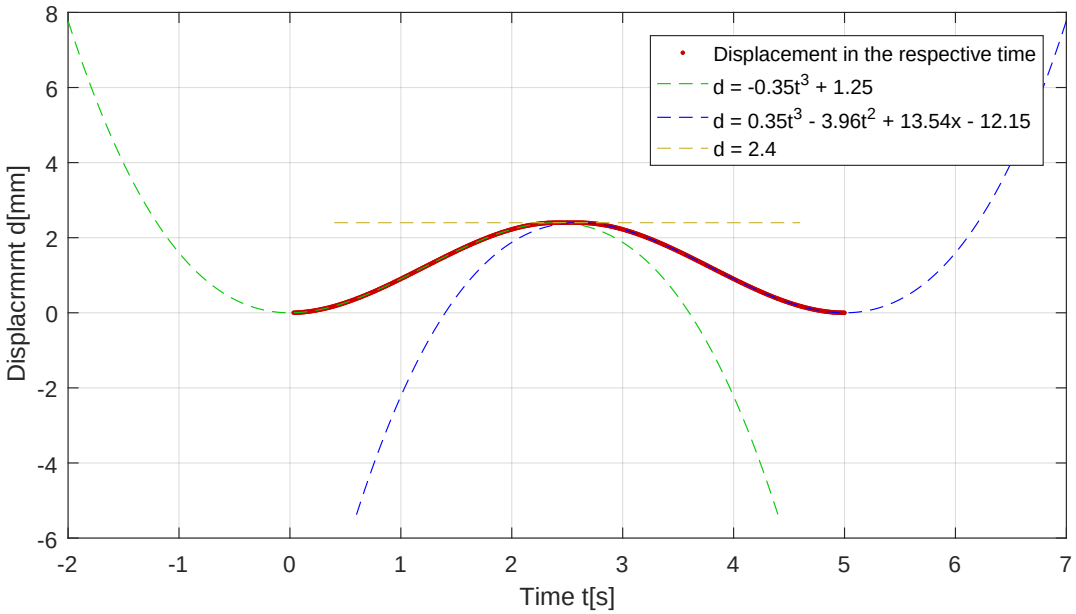

Fig. A.1: Positioning of mechanism in MSC ADAMS. The step function determined by cubic polynomial was used

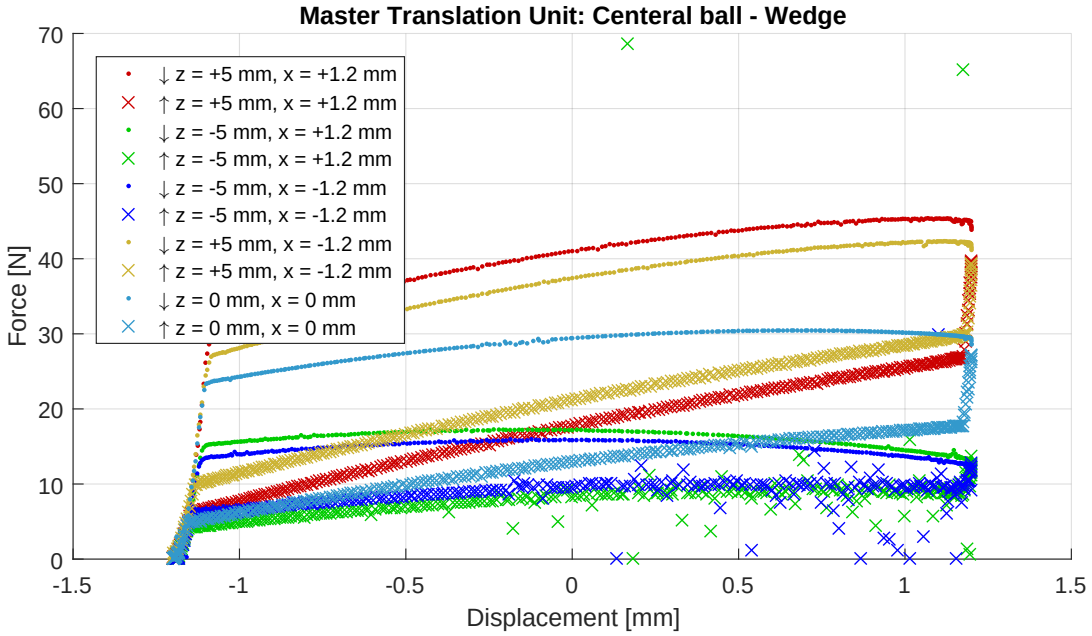

Fig. A.2: Magnitude of force in the contact between the central ball and the wedge in MTU in a varied positions and directions of movement among the mechanism. The ↑ and ↓ stands for increasing and decreasing displacement, respectively

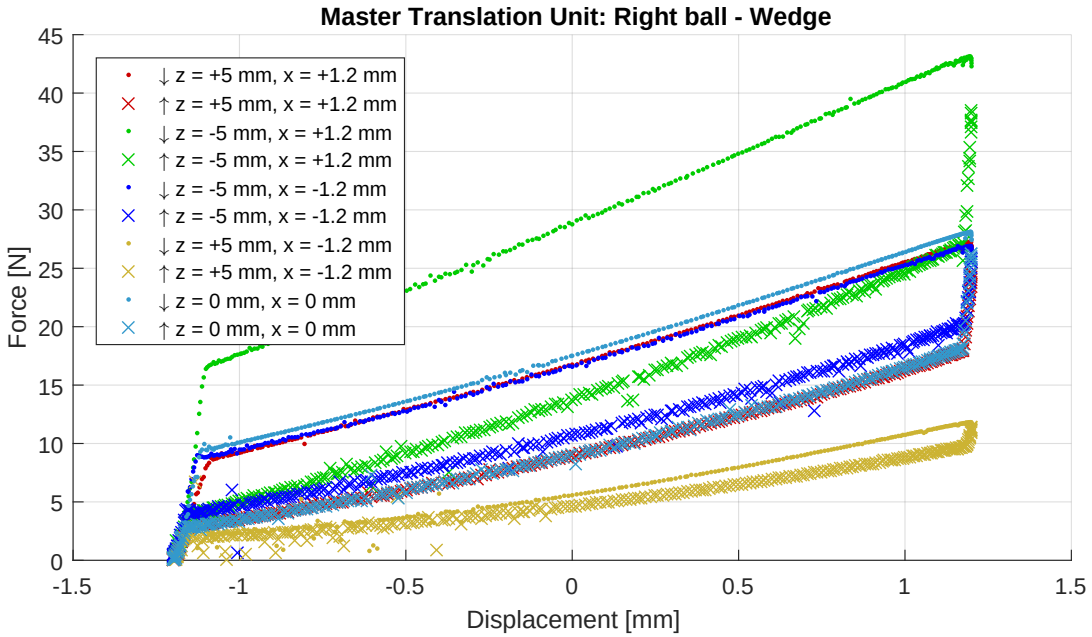

Fig. A.3: Magnitude of force in the contact between the right ball and the wedge in MTU in a varied positions and directions of movement among the mechanism. The ↑ and ↓ stands for increasing and decreasing displacement, respectively

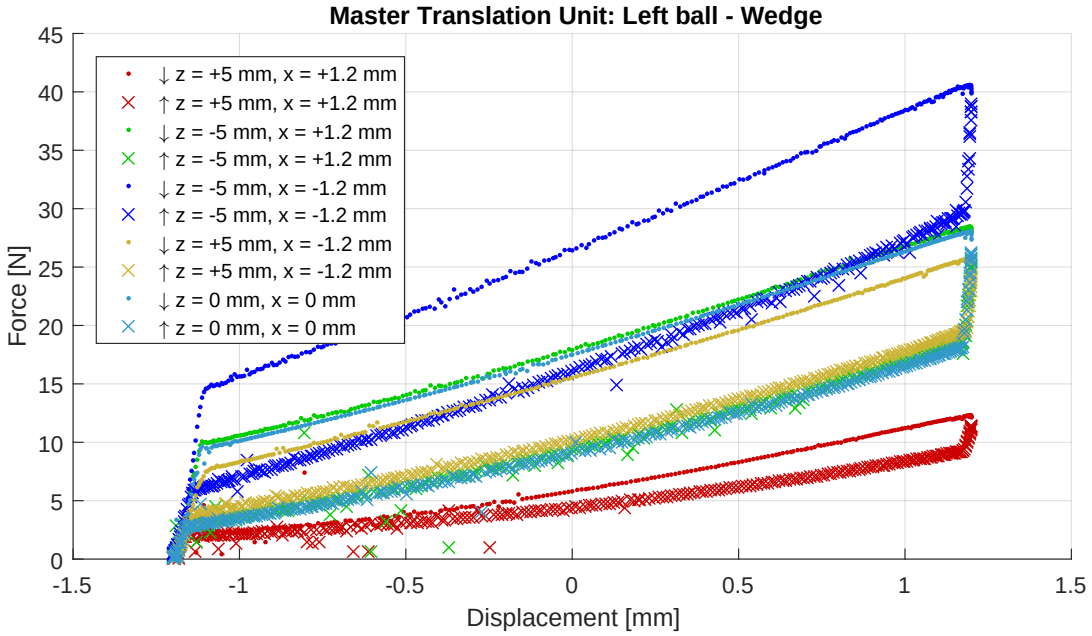

Fig. A.4: Magnitude of force in the contact between the left ball and the wedge in MTU in a varied positions and directions of movement among the mechanism. The ↑ and ↓ stands for increasing and decreasing displacement, respectively

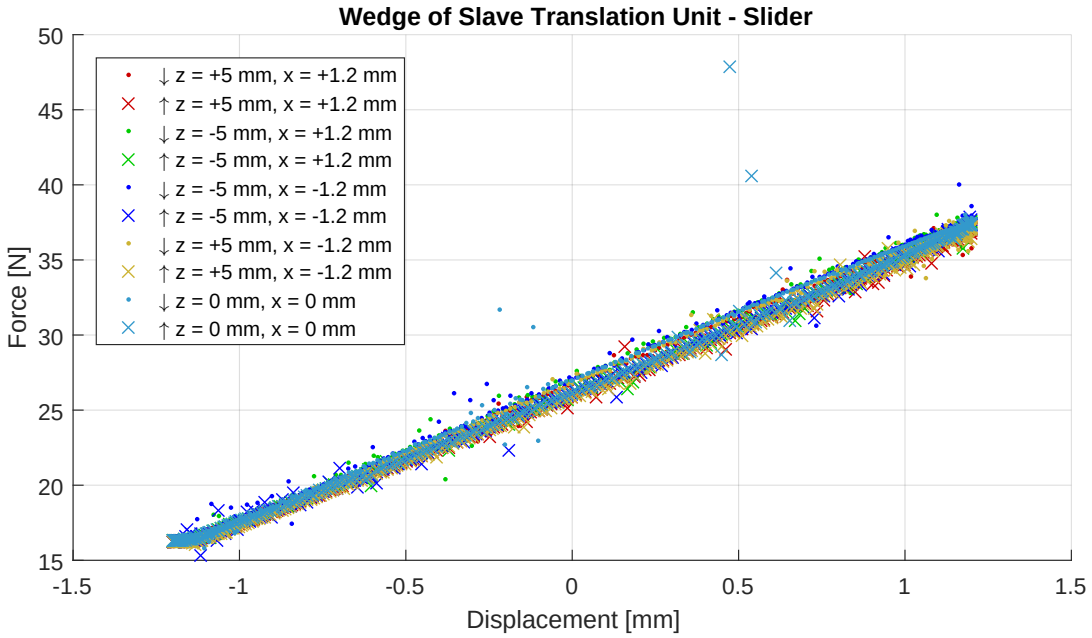

Fig. A.5: Magnitude of force in the contact between the wedge of STU and slider in a varied positions and directions of movement among the mechanism. The ↑ and ↓ stands for increasing and decreasing displacement, respectively

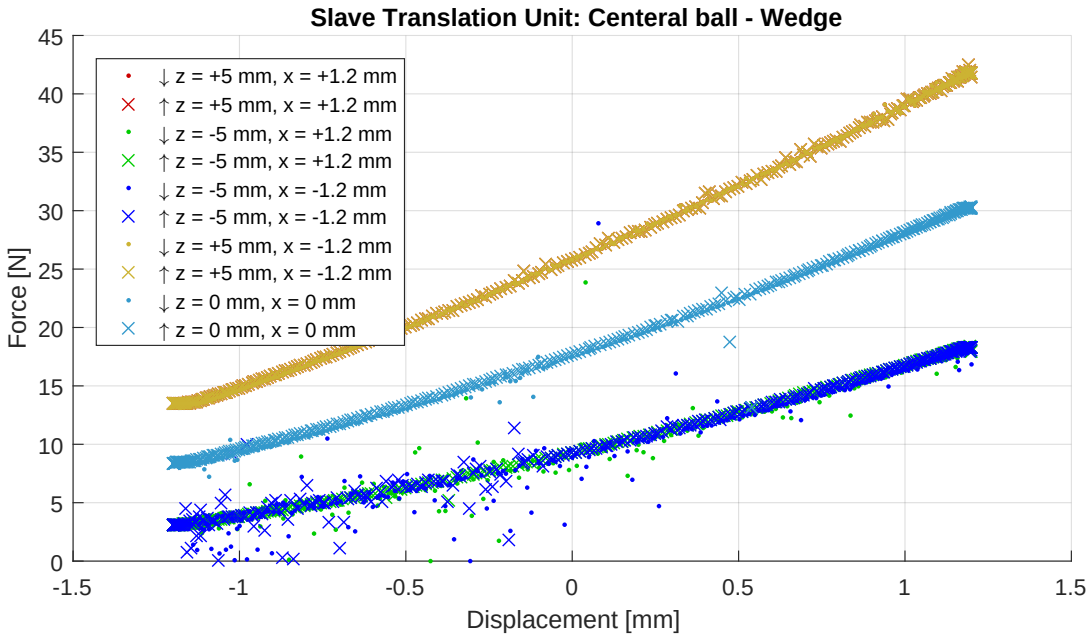

Fig. A.6: Magnitude of force in the contact between the central ball and the wedge in STU in a varied positions and directions of movement among the mechanism.The ↑ and ↓ stands for increasing and decreasing displacement, respectively

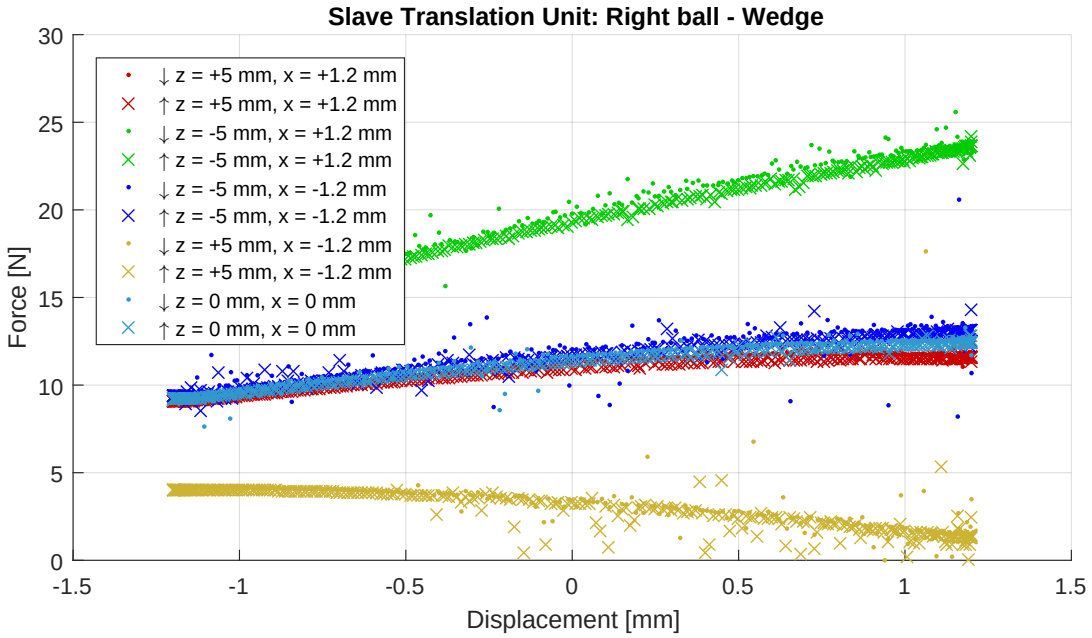

Fig. A.7: Magnitude of force in the contact between the right ball and the wedge in STU in a varied positions and directions of movement among the mechanism. The ↑ and ↓ stands for increasing and decreasing displacement, respectively

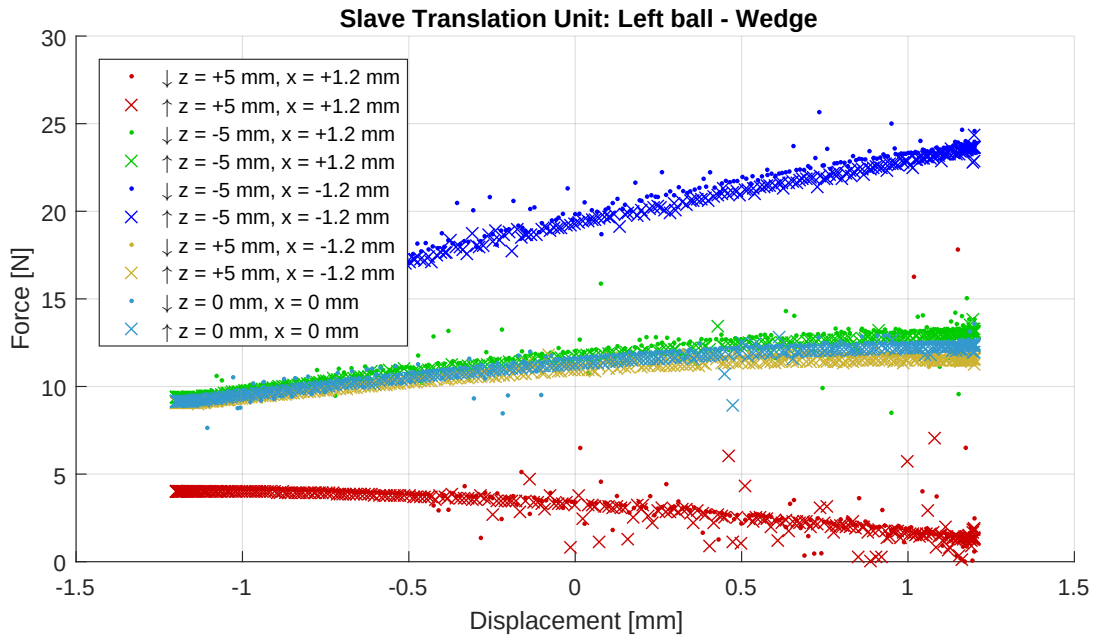

Fig. A.8: Magnitude of force in the contact between the left ball and the wedge in STU in a varied positions and directions of movement among the mechanism. The ↑ and ↓ stands for increasing and decreasing displacement, respectively

B Attached CD content

- `/` ..... the root folder of the CD
  - `Hlavní dokument.pdf` ..... The main document of this thesis in pdf
  - `Drawings` ..... Selected technical drawings of mechanical parts
    - `V-02658.pdf`
    - `V-02639.pdf`
    - `V-02630.pdf`
    - `V-02620.pdf`
    - `V-02617.pdf`

C List of attached technical drawings

Title	Part number	paper size
Těsnící vložka	V-02658	A4
Klín	V-02639	A3
Justážní hřídel	V-02630	A4
Hřídel horizontální jednotky	V-02620	A3
Příruba universálního vstupu-výstupu	V-02617	A2